PERSPECTIVES

The periodic table and the physics that drives it

Peter Schwerdtfeger⬤, Odile R. Smits and Pekka Pyykkö⬤

Abstract | Mendeleev's introduction of the periodic table of elements is one of the most important milestones in the history of chemistry, as it brought order into the known chemical and physical behaviour of the elements. The periodic table can be seen as parallel to the Standard Model in particle physics, in which the elementary particles known today can be ordered according to their intrinsic properties. The underlying fundamental theory to describe the interactions between particles comes from quantum theory or, more specifically, from quantum field theory and its inherent symmetries. In the periodic table, the elements are placed into a certain period and group based on electronic configurations that originate from the Pauli and Aufbau principles for the electrons surrounding a positively charged nucleus. This order enables us to approximately predict the chemical and physical properties of elements. Apparent anomalies can arise from relativistic effects, partial-screening phenomena (of type lanthanide contraction) and the compact size of the first shell of every l-value. Further, ambiguities in electron configurations and the breakdown of assigning a dominant configuration, owing to configuration mixing and dense spectra for the heaviest elements in the periodic table. For the short-lived transactinides, the nuclear stability becomes an important factor in chemical studies. Nuclear stability, decay rates, spectra and reaction cross sections are also important for predicting the astrophysical origin of the elements, including the production of the heavy elements beyond iron in supernova explosions or neutron-star mergers. In this Perspective, we critically analyse the periodic table of elements and the current status of theoretical predictions and origins for the heaviest elements, which combine both quantum chemistry and physics.

In 1869, Dmitri Ivanovich Mendeleev ordered the known elements into what he termed the 'periodic table of the elements' (PTE) on the basis of their increasing atomic weight and chemical similarity[1]. Mendeleev's PTE was proposed 5 years after Lothar Meyer had organized the 28 known elements into a table, of which six columns were labelled with valence number and five rows with atomic weight (see BOX 1 and, for a historical account, see REFS[2–8]).

Mendeleev not only correctly identified several of the then unknown elements, such as Ge, Sc, Ga and Tc — that were subsequently discovered in 1876, 1879, 1886 and 1937, respectively — but also corrected some erroneous atomic weights, such as for Be, In, Ce and U. FIGURE 1 shows a collection of PTEs, including an 1885 version of a

wall-hanging PTE (FIG. 1a). Mendeleev had no knowledge of the internal structure of an atom or nucleus; a more detailed picture started to emerge only in 1911 with Ernest Rutherford's discovery of the atomic nucleus. The development of the PTE over the past 150 years is nicely illustrated at the Internet Database of Periodic Tables. In the most recent version of the PTE (FIG. 1c), elements are ordered according to their atomic number Z (the number of protons inside the nucleus), thus avoiding irregularities in mass numbers due to the different numbers of neutrons inside the nucleus. As of today, 118 elements are experimentally known, with the most recent additions to the PTE being the main-group elements from Nh ($Z = 113$) to Og ($Z = 118$), thus successfully completing the seventh period of the PTE.

The PTE is the most fundamental pillar of chemistry[4]: molecules, large or small, are all made of interacting atoms from the PTE, forming various types of chemical bonds. To cite Shaik and colleagues, "The periodic table gave rise to a central paradigm, which did for chemistry what Newton had done for physics and Darwin for biology"[7]. Questions naturally arise from this ordering system: what are the underlying (quantum) principles of the PTE? Where does the PTE end from an electronic or nuclear point of view? How far can we go in the synthesis of new elements and isotopes both in the laboratory and in the interstellar environment? Can we keep using the same approach to unambiguously place the elements with nuclear charge $Z > 118$ into the PTE[9] (as, for example, suggested in 2011 by one of the authors and shown in FIG. 1c)?

In this Perspective, we address fundamental questions concerning the PTE and discuss the current status of this field from a quantum theoretical point of view[10,11]. We describe the underlying physical principles that shape the PTE, including the elements up to a certain critical nuclear charge ($Z \approx 172$). We focus on anomalies in chemical and physical properties, rather than on similarities between the elements within a certain group. Furthermore, we discuss the astrophysical origin and nuclear stability of the elements, including the most recent developments in the field of nuclear-structure theory.

From fundamental physics to the PTE
The PTE is as fundamental to chemists as the table of elementary particles is to physicists (FIG. 2). We all know that atoms interact to form chemical bonds. Note that the term 'chemical bond' is a fuzzy concept, because it does not strictly correspond to a quantum-mechanical observable. However, it is a useful concept derived from quantum-theoretical principles[12–14] and can be attributed to the lowering of the electronic kinetic energy, concomitant with the constructive interference between the constituents in the molecular wavefunction[15,16]. In much the same way, fermions (spin 1/2 particles, like the electron) interact through (gauge) fields described by the exchange of bosons

---

Box 1 | A bit of history: Dmitri Ivanovich Mendeleev and Lothar Meyer

The International year of the Periodic Table (IYPT) in 2019 commemorated the 1869 papers of Dmitri Ivanovich Mendeleev (see the figure, panel **a**). Five years earlier, Lothar Meyer (see the figure, panel **b**) had introduced in his 1864 book *Die Modernen Theorien der Chemie* (1st edn., p. 137), a 28-element table with six columns labelled by valence numbers and five rows with increasing atomic weight, correcting the Te/I mass anomaly[293]. Meyer's columns correspond to the groups 1–2 and 14–17. He did not claim new elements and did not have groups 3–13 or explicitly mention periodicity. He also attributed valencies to certain transition metals from modern groups 4–12. Meyer later commented (translated from German): "Recently, Mendeleyeff has shown that such an arrangement can already be obtained by simply arranging atomic weights of all elements without random selection into a single row according to the size of their numerical values, decomposing such a row into sections and putting them together in the unmodified sequence. The table shown below is essentially identical to that given by Mendeleyeff"[294–296]. We refer to an excellent historical discourse into Lothar Meyer's life and work and comments on this issue by Gisela Boeck[297].
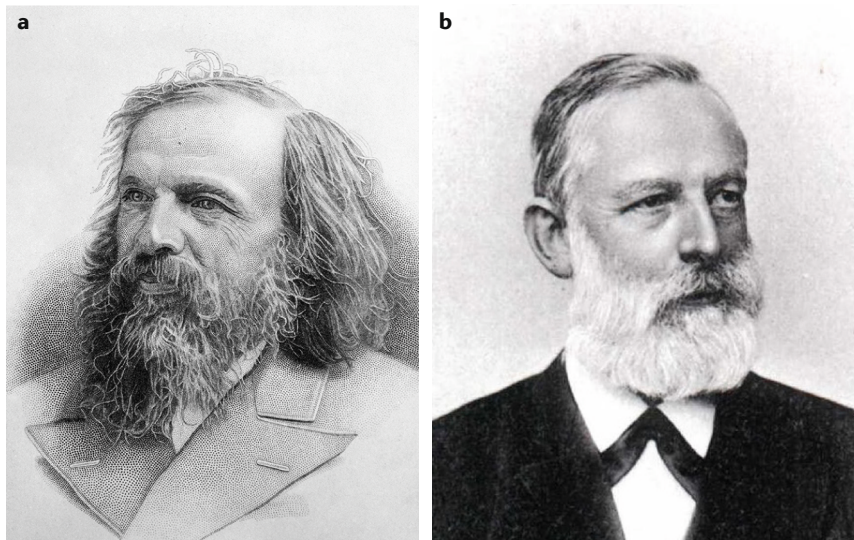
Credit for figure part **a**: Granger Historical Picture Archive/Alamy Stock Photo. Credit for figure part **b**: The History Collection/Alamy Stock Photo.

(integer-spin particles). Bosons are the carriers of the fundamental forces known in nature and are accurately described (as far as we know) by the Standard Model. Here, the electromagnetic force is mediated by photons, the weak force responsible for the β-decay in nuclei and the existence of the heavier elements in the PTE are mediated by charged ($W^{\pm}$) and neutral (Z) bosons, and the strong force responsible for the existence of protons, neutrons and nuclei is mediated by gluons. The fourth fundamental interaction in nature, the gravitational force, has yet to be unified with the Standard Model, which represents one of the major challenges in physics. If the gravitational force can be quantized, the carriers of this force would also be bosons, so-called gravitons. All four fundamental forces are important for the astrophysical production and existence of the elements in the PTE and, ultimately, for the existence of life in our universe. Finally, the Higgs spin-zero boson provides the mass for the particles in the Standard Model (except, perhaps, for the neutrinos).

Why do we mention the fundamental principles of particle physics here? Because the concept behind the PTE is strongly connected to fundamental physics involving not only atomic and molecular but also particle and nuclear physics, two fundamental aspects that are usually not part of mainstream chemistry teaching and might not be familiar to all chemists. Starting with the electronic shell structure (the nuclear structure is discussed further below), the population of the PTE is governed by both the Pauli and the Aufbau principles. At a more fundamental level, the spin-statistics theorem in physics (formulated by Fierz and Pauli[17]) demands that, for fermions — such as the electron — the many-particle wavefunction $\psi(\mathbf{r}_i, t)$ has to be antisymmetric with respect to the permutation of two particles, k and j, from which the Pauli principle in a single-particle picture (mean-field theories such as Hartree–Fock or Kohn–Sham) follows. For chemists, this simply means admitting only one electron per single-particle state. This mean-field picture then leads to the famous

Aufbau principle introduced by Bohr and Pauli that, together with Hund's rule, is considered as the second building block of the PTE, after the atomic-number ordering.

Chemical behaviour is the third most important criterion that guides the order of elements in the PTE and an essential tool for all chemists. Similarities in the valence-electron configurations for two atoms usually imply similar chemical properties, although subtle shell-structure effects can lead to anomalies in the chemical and physical behaviour discussed below. The electron configuration of a multi-electron atom or, more precisely, the configuration list including occupation numbers for individual one-electron states, is (together with the atomic number) an important parameter for placing an element into the PTE. The Schrödinger equation gives us the eigenfunctions in the form of complex many-electron wavefunctions and the corresponding eigenstates (that is, the spectrum) of an atom, molecule or a condensed phase. The solutions of the Schrödinger equation inform us on physical properties (such as the dominant electron configuration), which give us important insights into the chemical behaviour of the elements[18]. Together with thermodynamics and statistical physics, this differential equation lies at the very heart of chemistry.

From the solution of the stationary Schrödinger equation for a hydrogen-like atom, we know that (nlm_l) states with the same principal quantum number n are energetically degenerate. In the relativistic case, this degeneracy is partially lifted owing to spin–orbit coupling, which can become very large for heavy elements, leading to the $l > 0$ levels split into levels of $j = l \pm 1/2$. Quantum electrodynamics (QED) further lifts the degeneracy between the s and $p_{1/2}$ levels by a small amount. This so-called Lamb shift is tiny, 4.372×10^{-6} eV for the $2s$–$2p_{1/2}$ splitting in the hydrogen atom, but can approach chemical relevance for heavy elements[19,20], such as Au or Og[19–21].

Degeneracies are further broken in the screened Coulomb potential of multi-electron atoms, for example, following the Aufbau principle, the $2s$ levels are filled before the $2p$ levels. Slater was the first to extend systematically the one-particle solutions of the Schrödinger equation to a multi-electron system[22] following earlier work by Zener[23]. In the so-called mean-field model for a multi-electron atom, each electron is moving in the field generated by all other electrons and the nucleus experiencing a reduced nuclear charge, $Z^{\text{eff}} = Z - \sigma$, which is due to the shielding

(or screening) by all the other electrons and expressed by the screening constant σ. Slater's rules provide numerical values for σ in multi-electron systems that enable the approximate calculation of the total electronic energy. The idea of a screening effect leads to the lifting of degeneracies and explains why the $4s$ level is occupied before the $3d$ levels (for example, in the case of K, $Z^{eff} = 2.20$ for the $4s^1$ and $Z^{eff} = 1.00$ for the $3d^1$ valence configurations). Slater's approach can be seen as the first successful quantum-theoretical attempt to place the elements correctly into the PTE using the Aufbau principle. It places the electrons obeying the Pauli principle into the levels experiencing the highest effective nuclear charge first. However, if the gap between

two one-electron levels is smaller than the exchange-energy correction, the lowest energy is obtained for the high-spin configuration. Despite its early success, the original Slater rules have their limitations. They did not explain why the $2s$ level is occupied before the $2p$ level, as these shared the same screening factor σ, or more subtle differences in electron configurations, as found, for example, in the group-10 elements: Ni ($3d^8 4s^2$), Pd ($4d^{10}$), Pt ($5d^9 6s^1$) and Ds ($6d^8 7s^2$). However, it is not important which screened-Coulomb potential is chosen for the Aufbau discussion[8]. For example, in the past, the Thomas–Fermi model was used to determine the atomic number at which l-electrons for a given l_{max} first appear[24–27].

A far more accurate determination of electron configurations is achieved using mean-field methods such as relativistic Hartree–Fock or Kohn–Sham density functional theory (DFT). With these methods, one can easily obtain low-lying electronic states associated with dominant electron configurations and effective nuclear charges for a specific electronic shell. For example, Hartree defines the screening constant as $\sigma_{nl} = Z - \langle r \rangle_{nl}^{H} / \langle r \rangle_{nl}$ for a specific nucleus of charge Z and shell (nl), where $\langle r \rangle_{nl}^{H}$ is the unscreened hydrogenic value, which can be obtained analytically (for the relativistic case, we simply extend it to the shell with quantum numbers (nlj))[28]. From relativistic Hartree–Fock calculations of Li, we obtain $Z_{2s}^{eff} = 1.55$ and $Z_{2p}^{eff} = 1.04$,
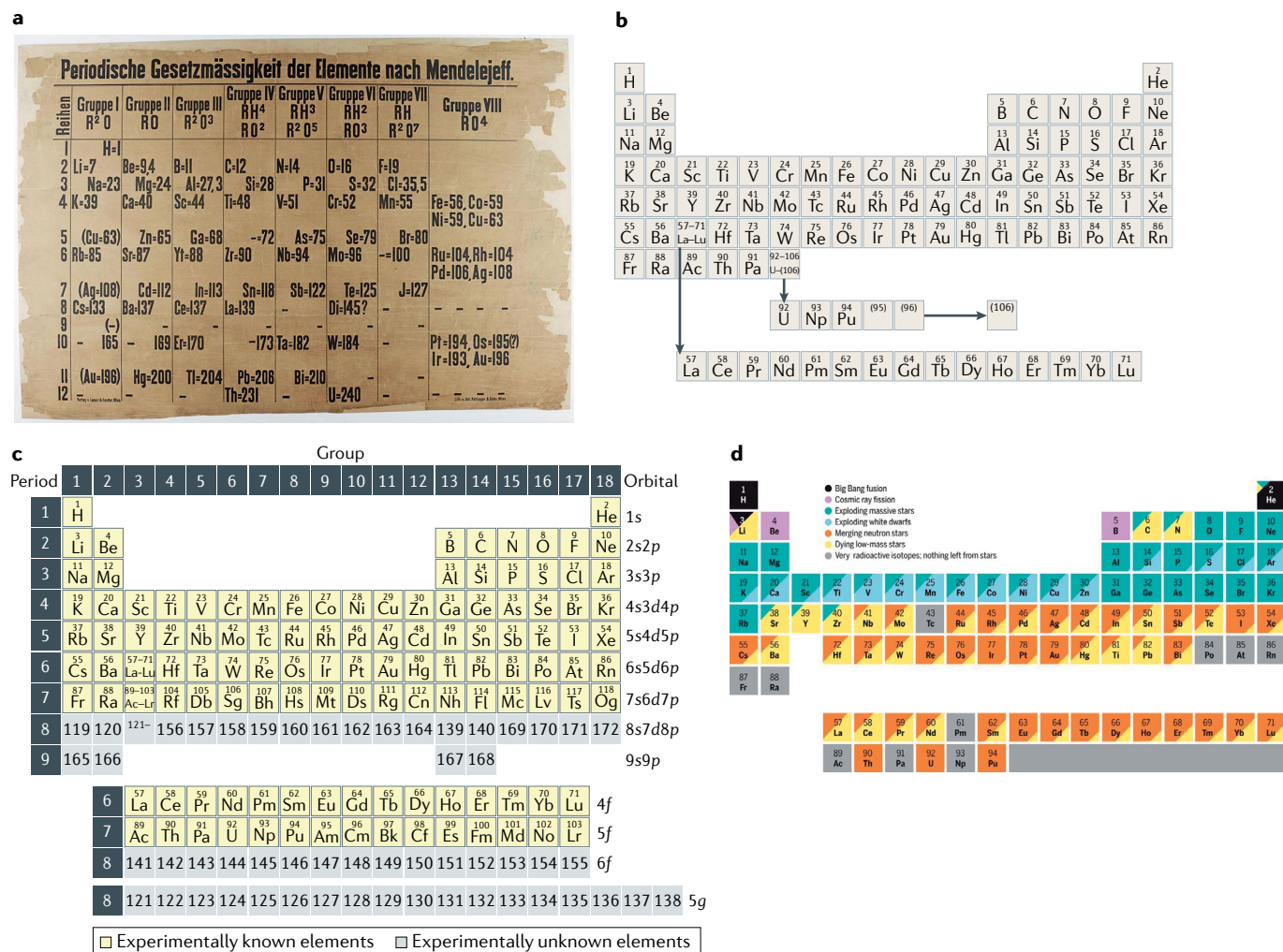
Fig. 1 | **Periodic tables. a** | Early example of a periodic table of elements (PTE). This PTE was originally printed in 1885 and purchased in 1888 by the University of St. Andrews, where it is currently exposed. **b** | A 1942 PTE by Glenn T. Seaborg. In this version, the $5f$ elements were not introduced yet, Th is shown in the group below Hf, Pa below Ta and U below W. The actinide series got its proper place in the PTE in 1944. **c** | PTE in which a single electron configuration is assigned to each atom[9]. The elements in yellow are now experimentally known, as opposed to those in grey. The number of valence electrons is given by the group number (G) (groups 1–12) or G−10 (groups 13–18). The length and the location of the rows reflect both the chemistry of the elements and the shell structure of their atoms. Note the suggested location of a putative $5g$ series. **d** | PTE showing the predicted origin of elements in the Solar System. Elements beyond Pu are not included. Part **a** is courtesy of the University of St Andrews Library, ms39012, REF.[280]. Part **b** is adapted from REF.[281], World Scientific. Part **c** is adapted from REF.[282], Springer Nature Limited. Part **d** is reprinted with permission from REF.[283], AAAS.
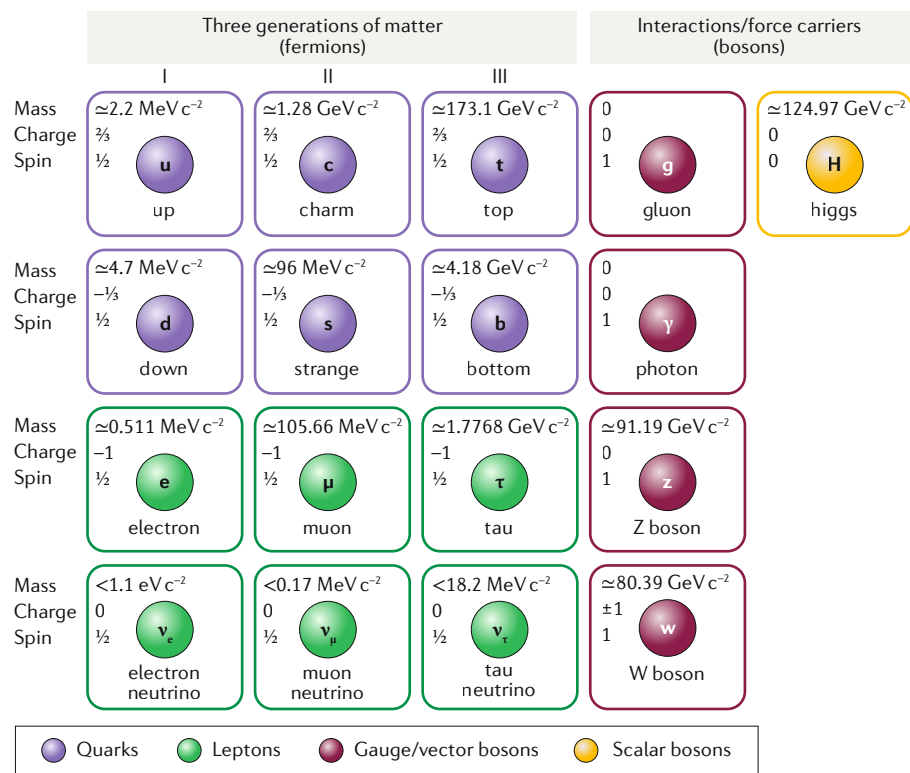
Fig. 2 | **The Standard Model of fundamental particles.** The Standard Model of fundamental particles serves physicists in the same way as the periodic table of elements serves chemists, thus, we can consider the Standard Model as 'the physicist's periodic table'. It contains the elementary particles in nature as we currently know. These are grouped into fermions and bosons, the latter being responsible for the fundamental forces in nature (the gravitational force is not included here). The corresponding anti-particles (not shown here) have the same mass as far as we know but opposite charge. Note that, in this Perspective, we use energy units of eV for spectroscopic and nuclear properties (1 eV = 0.4853075 kJ mol^{-1}). Masses are given in energy units through $E = mc^2$ and 1 amu = 931.49410242 MeV. For bond energies, we use kJ mol^{-1}. Figure drawn from data in REFS[45,284].

and for K, we obtain $Z_{4s}^{eff} = 4.59$ and $Z_{3d}^{eff} = 1.10$ (REF.[29]), which are qualitatively correct. Even if we use post-Hartree–Fock theory and include electron correlation, for example, by a configuration interaction treatment that accounts for the mixing of configuration states, we can still determine the dominant configurations and try to assign an approximate electron configuration to an atom. This simplified picture can, however, break down if the energy levels are not well separated and the spectrum becomes dense owing to quasi-degeneracies — ultimately, the correct ground state can only be determined by solving the Schrödinger equation or, more precisely, the Dirac equation that includes important QED effects (BOX 2).

Let us look again at the electron configurations in the group-10 elements. Information about electronic states and configurations are collected in FIG. 3. The three dominant configurations — $[(n-1)d^8 ns^2]$, $[(n-1)d^9 ns^1]$ and $[(n-1)d^{10}]$ — lead to a total of 13 states separated

by small energy differences as shown in FIG. 3a. However, this does not prevent us from placing these elements correctly into group 10 of the PTE.

Moving to group 11, of the three ns^1 coinage-metal atoms (Cu, Ag and Au), only Ag behaves as chemically expected[30]. Cu is anomalous, having a radially nodeless and, therefore, compact, $3d$ shell. Au is anomalous for both its lanthanide contraction owing to the filling of the $4f^{14}$ shell and (even more so) strong relativistic effects. Ag in between has a d-shell node and only moderate relativistic effects. Rg even changes its ground state to $d^9 s^2$ owing to a strong relativistic $7s$ stabilization.

Despite the theoretical limitations of using electron configurations due to configuration mixing, we can safely place all known 118 elements into the PTE using the Aufbau principle (Edward G. Mazurs presented a periodic table in 1955 classified later as Subtype IIIC3-6b in which he correctly placed the elements into the PTE up to $Z = 120$ (REFS[31,32]).

As a matter of interest, the Aufbau principle follows the empirical rule proposed by Madelung in 1926 (REFS[33,34]) and Janet in 1930 (REF.[35]), as shown in FIG. 3b, and used early on by Sommerfeld[36] to fill the electronic configurations up to Rn. The Madelung–Janet (or diagonal) rule states that, when considering consecutive neutral atoms, electrons are assigned to one-particle levels in order of increasing $(n + l)$ value and, for states of equal $(n + l)$, the electrons are assigned first to the lower n value. For a detailed account on the Madelung–Janet rule, see REF.[37]. This rule is remarkably well fulfilled throughout the PTE, with only a few exceptions in the superheavy-element region because of strong relativistic effects. Nevertheless, the putative placement of the superheavy elements beyond $Z = 120$ by one of the authors[9] requires further investigations to correctly predict the electronic ground state and associated dominant configurations together with their chemical similarities to their lighter congeners — a major challenge for modern quantum chemistry. For example, Nefedov and colleagues performed multi-configuration Dirac–Fock calculations for the superheavy elements with $Z = 119$–164 (REF.[38]). They showed that a major single configuration can still be assigned for these elements, despite the fact that the $5g$, $6f$, $7d$ and $8p$ levels become close in energy. They further predict the $5g$ occupation in neutral atoms to start at $Z = 125$.

Despite the huge success of the Madelung–Janet rule, the most appropriate definition of the start and end points of the lanthanide and actinide series remains a matter of dispute[39,40]. Inserting the lanthanides La–Yb and actinides Ac–No between groups 2 and 3, and Lu [$4f^{14}5d^1 6s^2$] and Lr [$5f^{14}7p^1 7s^2$] (note the difference in the occupation of p and d levels between the two elements) into group 3 fulfils the Madelung–Janet rule and results in a more natural placement of these elements into the PTE. However, placing La [$5d^1 6s^2$] and Ac [$6d^1 7s^2$] into group 3 and the series Ce–Lu and Th–Lr afterwards has the advantage of keeping La and Ac as the first elements of the lanthanide and actinide series to which they give their names. In a set of molecules, Xu and Pyykkö[41] found that Lu and Lr behave in a very similar way. Moreover, the placement of the $4f$-to-$6f$ and the $5g$ elements in FIG. 1c keeps the group number, G, equal to the number of valence electrons. We are not delving further into discussions of chemical similarities between the two different definitions of the group 3 elements, as there

are many different opinions on this[40,42]. The International Union of Pure and Applied Chemistry (IUPAC) conveniently avoids this controversy by leaving the two positions in periods 6 and 7 of group 3 empty and listing 15 instead of 14 elements for the lanthanides and actinides, thus counting from f^0 to f^{14}. Fuzzy concepts like chemical similarities or electron configurations do have their limits, but, in our opinion, do not reduce the importance of the PTE.

Periodic trends and relativistic effects

It has become (almost) a doctrine in chemistry that elements placed in the same group of the PTE show similar chemical and physical behaviour. Similarities and differences are based on the comparison of measurable quantities, either through experimental observables or through their calculations using the corresponding quantum-mechanical (self-adjoint) operators, if necessary to the highest accuracy available within a certain theory. A detailed discussion on the numerous similarities observed is beyond the scope of this Review. For recent accounts, see REFS[43,44] and for main-group elements, see REF.[18]. Instead, we focus on some irregularities and anomalies within the PTE that arise from shell-structure and relativistic effects.

1s elements. We start our discussion by mentioning the two most abundant elements in our universe, H and He, synthesized directly in the primordial nucleosynthesis roughly 10 seconds to 20 minutes after the Big Bang[45]. These are placed into groups 1 and 18, respectively, although their chemical and physical behaviour is quite distinct compared with their heavier homologues in the PTE. Hydrogen has unique properties and functions: from hydrogen, we get water and biomolecules important for life on our planet. Watson–Crick pairing is a prime example in which hydrogen bonding is required for the stability of DNA[46]. Furthermore, let us compare the structure of benzene and its associated rich aromatic chemistry to C_6Li_6, which consists of C_2^{2-} fragments strongly aggregated through Li bridges[47]. We can also consider the recent discovery of superconductors in hydrogen-rich phases[48–50] and the search for metallic, high-pressure phases of pure hydrogen important for understanding the physics of large-sized planets such as Jupiter[51].

Although He is the most abundant element in our universe (but rare on our planet), its chemistry is very limited. Needless to say that the electron

configuration of He is [$1s^2$] — with the highest ionization potential of any element (24.587387 eV)[52] — whilst for the other noble gases, it is [np^6]. Both isotopes ^{3,4}He at low temperatures exhibit a distinct quantum nature and special phases in the bulk. Because of its chemical inertness, He fits rather into group 18 than into group 2 of the PTE, although we note the existence of gas-phase cations, such as HeH^+, or metal helides, such as VHe^{3+}, YHe^{3+} or $AlHe^{3+}$ (REFS[53–55]), and the observed high-pressure electride compound Na_2He[56]. This is a prime example in which chemical similarity wins over electron configuration.

Although H and He clearly separate from the rest of the PTE, almost every chemist agrees that we can leave these elements in their current place in the PTE, keeping their distinctive quantum nature in mind.

Primogenic shell effect. Continuing with trends within a group of the PTE, we note the compact size of the shells with every first-appearing l-value (termed primogenic[57]

or kainosymmetric effect, the special nature of which was pointed out by Shchukarev in 1971 (REFS[58,59]). The primogenic effect has far-reaching consequences; for example, it explains the existence of P_4 and not of N_4 (REF.[60]) or, more importantly, the quite distinct chemistry of C versus Si[61] and why life based on Si instead of C may not exist. This effect can be clearly understood by comparing the valence shell radii (in Å) and screening constants σ of C and Si (obtained from Hartree–Fock calculations): $\langle r \rangle_{2s}^C = 0.839$ Å, $\sigma_{2s}^C = 2.22$, $\langle r \rangle_{2p}^C = 0.921$ Å, $\sigma_{2p}^C = 3.13$; $\langle r \rangle_{3s}^{Si} = 1.164$ Å, $\sigma_{3s}^{Si} = 7.86$; $\langle r \rangle_{3p}^{Si} = 1.473$ Å, $\sigma_{3p}^{Si} = 9.51$[29]. Similarly, the first-row transition elements have a compact $3d$ shell and, often, their chemical behaviour differs to that of the heavier congeners. For example, RuO_4, OsO_4 and even HsO_4 are experimentally known[62], but FeO_4 is not (only its reduced states $[FeO_4]^{2-}$ and $[FeO_4]^-$ are known[63]). Trends down a group are further influenced by relativistic effects, which can change completely the chemical behaviour of the heavier elements.

Box 2 | The many-electron Dirac–Fock–Breit Hamiltonian

The many-electron Dirac–Fock–Breit Hamiltonian can be considered a chemist's 'Theory of Everything'.

The many-electron Hamiltonian can be expressed as the sum of one-electron (h_i) and two-electron (h_{ij}) Hamiltonians:

$$H = \sum_i h_i + \sum_{i<j} h_{ij}. \tag{1}$$

The non-relativistic one-particle Hamiltonian would be (in atomic units):

$$h = T + V_n, \quad T = -\frac{1}{2}\nabla^2 \tag{2}$$

with T being the kinetic energy, V_n the potential energy and ∇^2 the Laplace operator. The non-relativistic two-particle Hamiltonian would be:

$$h_{ij} = 1/r_{ij} \tag{3}$$

where r_{ij} is the distance between the two particles.

The one-particle Dirac Hamiltonian (h_D) takes into account relativistic effects and reads as:

$$h_D = c\vec{\alpha} \cdot \vec{p} + \beta c^2 + V_n, \quad \vec{p} = -i\vec{\nabla}, \tag{4}$$

where α_k ($k = 1, 2, 3$) and β are Dirac matrices, $\vec{p}$ is the momentum and $c = 137.035999$ au is the speed of light.

The relativistic two-particle Hamiltonian (h_B) can be obtained by including in Eq. 3 the Breit interaction (here, chosen as frequency-independent) that describes the magnetic electron–electron interactions and retardation effects.

$$h_B = -\frac{1}{2r_{ij}}\left[\vec{\alpha}_i \cdot \vec{\alpha}_j + (\vec{\alpha}_i \cdot \vec{r}_{ij})(\vec{\alpha}_j \cdot \vec{r}_{ij})/r_{ij}^2\right]. \tag{5}$$

In correlated calculations, electron-like projection operators, P, should be added:

$$h_{ij}^{eff} = P h_{ij} P. \tag{6}$$

Quantum electrodynamics corrections can also be added to achieve higher accuracy. For more details, see REF.[30].
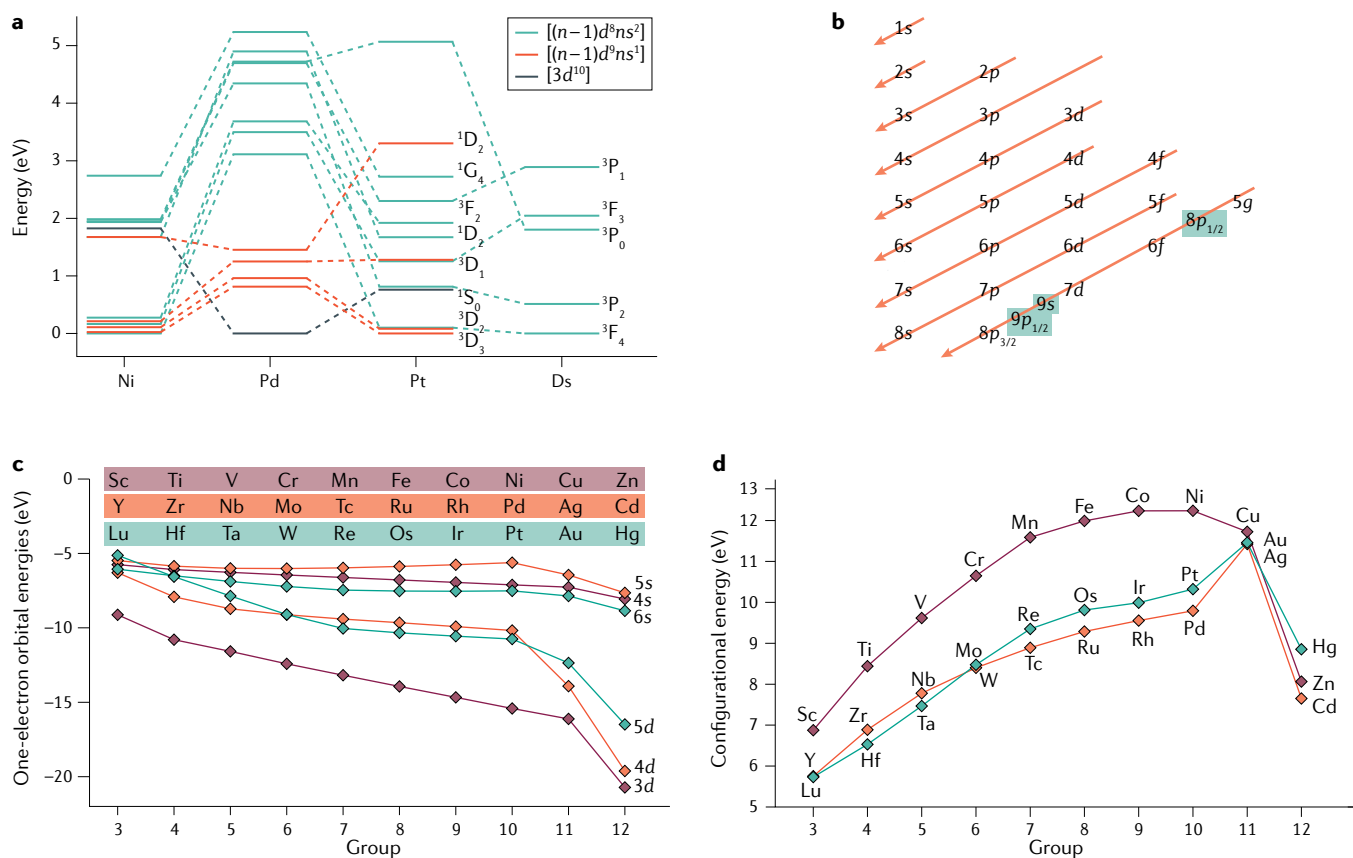

Fig. 3 | **Electronic states and configurations. a** | Energy levels for the dominant configurations of the group-10 elements as reported from the National Institute of Standards and Technology (NIST). Different colours are used to distinguish between the three different configurations: $[(n-1)d^8ns^2]$, $[(n-1)d^9ns^1]$ and $[3d^{10}]$. Note that, already for Pd, there are intruder states (not shown here) that arise from the $[(n-1)d^9np^1]$ configuration and mix with several of the low-energy states shown here. The same happens for the intruder states for Pt from the $[(n-1)d^9np^1]$ and $[(n-1)d^8ns^1p^1]$ configurations. For Ds, a dense spectrum arising from the $[6d^7_{5/2}7s^27p^1_{1/2}]$ configuration intrudes into the normal spectrum and only a few lines of even parity predicted by Lackenby and colleagues are given here. Thus, some configuration assignments (especially for the $^3P_0$ level) are approximate at best. Data shown here are from REFS[285,286]. **b** | Successive shell filling according to FIG. 1c, up to the heaviest element with $Z=172$ according to the Madelung–Janet rule. The anomalies in expected shell filling are highlighted in green. They result from strong relativistic stabilization effects of the s and $p_{1/2}$ shells at high nuclear charge. **c** | Orbital energies for the $3d$, $4d$ and $5d$ transition-metal atoms (in eV). **d** | Configuration energies for the $3d$, $4d$ and $5d$ transition-metal atoms (in eV). Part **b** is adapted from REF.[131], CC BY 4.0 (https://creativecommons.org/licenses/by/4.0/). Data in parts **c** and **d** are from REF.[65].

Filling l-shells along a row of the PTE.
Turning to periodic trends along a specific row, 66.7% of the d-block elements (not including the transactinides) and 78% of the f-block elements have $nd^{G-2}(n+1)s^2$ and $(n-1)f^{G-2}(n+1)s^2$ electronic configurations, respectively, where G denotes the group number in the PTE. Some d-block elements prefer a greater d-population and some f-block elements prefer a single electron in the d-shell[64]. Nevertheless, different electron configurations lie close by in energy and we can successively fill the d-shell or f-shell using Hund's rule.

Allen and colleagues analysed the $(n-1)d$ and ns orbital energies for the transition elements[65]. Because the energies depend on the different ns populations (FIG. 3a), the concept of configuration energies ε_{CE} previously introduced by Allen[66] was used. Configuration energies for the transition elements can be defined as $\varepsilon_{CE} = -(p\varepsilon_s + q\varepsilon_d)/(p+q)$, where p and q are fractional occupation numbers for the s and d shells with orbital energies ε_s and ε_d, respectively. This approach considers configuration mixing in this orbital space and avoids anomalies in trends arising from changes in configurations along the transition-metal row. FIGURE 3c,d shows the results of these calculations and reveals some interesting trends.

We observe that the $(n+1)s$ shell comes at higher energy than the underlying nd shell and the valence s electrons are, therefore, more easily accessible. Furthermore, the s–d energy gap increases across a row, with a more prevalent increase for the first-row ($3d$) transition elements. The easy access of the s valence shell is seen as the main reason why all transition elements, except Sc, form divalent chlorides, MCl_2. However, the chemistry of the transition metals is far more complicated because the d subshell can contribute substantially to chemical bonding, especially for metals in higher oxidation states, even for the late transition elements as in the case of CuF_4^- (REF.[67]). For the third-row transition elements ($5d$) and fourth-row ($6d$) transactinides, the relativistic s-shell contraction becomes large, leading to an additional nuclear screening for the underlying d shell. This effect becomes particularly large for the groups 11 and 12 elements, as clearly seen in FIG. 3c,d, leading to well-known chemical and physical anomalies (see discussion below). Finally, for the $3d$ transition metals, we see a steep increase in configuration energies up to the element with half-filled d shell, Mn, defining a threshold between the early and late transition metals (for a more detailed discussion on this subject, see REFS[59,68]).

Relativity and the PTE. The Schrödinger equation, which has served the chemistry community extremely well for the past 50 years, emerges as the non-relativistic limit (speed of light $c \to \infty$) from its relativistic extension, the Dirac equation (BOX 2). The electronic Dirac equation did not come so easy to the discrete-basis quantum-chemistry community because of the appearance of a negative-energy continuum, the Dirac sea. This additional feature causes trouble in the treatment of elements with very high nuclear charge, $Z\alpha_{EM} > 1$, with α_{EM} being the fine-structure (or electro-magnetic coupling) constant defined as $1/\alpha_{EM} = 4\pi\varepsilon_0\hbar c/e^2 = 137.035999084(21)$[69]. Nevertheless, the enormous progress in this field over the past four decades has enabled us to deal efficiently with the electronic Dirac equation and to obtain very accurate solutions[70] (BOX 3).

Over the past few decades, we learned that relativistic effects are more important than originally thought. Valence electrons move slowly compared with the speed of light when they are far from the nucleus but fast when they are near the nucleus, especially for the heavy elements with high nuclear charge[71–74]. A close analysis shows that direct relativistic effects arise from the innermost region of the radial wavefunction (mainly from the K-shell ($1s$) range and, to a smaller extent, the L-shell range for all s orbitals), as well as from the spin–orbit splitting of all np orbitals[75,76]. Indirect relativistic contributions arise from the relativistic changes of the other orbitals. Relativistic effects are depicted in FIG. 4, and examples for both direct and indirect relativistic effects are illustrated in FIG. 4a,b.

Because of the direct relativistic effects, the nucleus becomes more screened, especially by the s and $p_{1/2}$ electrons that have a substantial electron density near the nucleus, thus lowering Z^{eff}. As a consequence, the more diffuse orbitals with higher angular momentum feel a weaker nuclear attraction, which results in their expansion and destabilization. An early example of the destabilization of the $5d$ shell of the Hg atom was reported by Mayers in 1957 (REF.[77]). In addition, spin–orbit coupling can become very large for the heavy elements (10 eV splitting between the $p_{1/2}$ and $p_{3/2}$ orbitals in Og with $Z = 118$)[78] (FIG. 4a,b). These large relativistic effects have been overlooked for a long time but are, perhaps, not unexpected, as these usually scale $\sim Z^2$ for the valence shells of analogous elements.

A detailed account on relativistic shell-structure effects in the d and f blocks

of the PTE has been given by Schwarz and colleagues[64]. Here, we focus on the two late transition metals, Au and Hg. It is now well established that these elements exhibit unusually large relativistic $6s$-orbital stabilizations (contractions) and indirect relativistic $5d$-orbital destabilizations (expansions) compared with their lighter congeners and to their neighbours to the left and right in the PTE, as first shown by Desclaux[29] and discussed in REF.[72]. A maximum stabilization of the ns shell can be observed for the $(n-1)d^{G-1}ns^1$ configuration in group 11 and for the $(n-1)d^{G-2}ns^2$ configuration in group 12, where G is the group number (FIG. 4c). The maximum in group 11 is well known[72] but perhaps not well understood[79]. It originates from the successive filling of the underlying $(n-1)d$ shell[64].

We can define relativistic effects for a specific atomic property P as $\Delta_R P = (P_R - P_{NR}) = \gamma_P(Z\alpha_{EM})^2 P_R$, where γ_P is the relativistic enhancement factor[64]. Although, down a group, valence shell relativistic effects mostly follow the expected $\sim Z^2$ behaviour, for group 11, the relativistic enhancement factor is very large and increases for the heavier elements. For example, we calculate γ_ε values for the orbital energy ε_{ns} in group 11 to be 0.573 (Cu), 0.616 (Ag), 0.731 (Au) and 0.795 (Rg) versus the values for group 12 of 0.428 (Zn), 0.480 (Cd), 0.616 (Hg) and 0.706 (Cn)[80]. The large relativistic enhancement factors for Au and Hg give rise to well-known anomalies in their chemical and physical behaviour, with some of these for Au being detailed in BOX 4. These anomalies are predicted to be even more pronounced in the superheavy element Rg, the chemistry of which remains largely unexplored, despite it being discovered in 1994 (REFS[10,81]). The ground state of Rg has a $6d^9 7s^2$ configuration, as opposed to a $6d^{10} 7s^1$ configuration, owing to the very large

relativistic $7s$ contraction that makes Rg as small as Cu in size[82–84]. It is clear from the data in BOX 4 that it is almost impossible to predict the physical and chemical behaviour of Rg from the properties of its lighter group members. In this case, we cannot count on the concept of chemical similarity within a group. We note, however, that relativistic effects heavily depend on the ns population of the elements in a molecule or the solid[85,86].

Turning to Hg in group 12, we also observe large relativistic effects that lead to anomalous physical and chemical properties[87]. Perhaps the most striking property is that Hg is the only elemental metallic liquid in the PTE (followed by Ga, which has a melting temperature of 29.76 °C), with a very high density of 13.5 g cm⁻³. Theoretical studies have shown that relativistic effects lower the melting point of Hg by more than 100 K (105 K and 160 K increases are predicted using atoms-in-molecules[88] and DFT calculations[89], respectively). Therefore, non-relativistic Hg would be solid at room temperature, similar to Cd. Also, the heaviest known group-12 element, Cn, has been predicted to be liquid at room temperature because of relativistic effects, with a rather narrow liquid range below the boiling point[90], supporting Pitzer's original hypothesis[91].

Because of the strong relativistic $7s$ contraction, Cn is predicted to be a semiconductor or even an insulator in contrast to Hg[90,92]. The unusually high superconducting transition temperature of Hg, in comparison with that of Zn and Cd, is also attributed to relativistic effects[93]: without relativity, Heike Kamerlingh Onnes would not have discovered superconductivity. Note that the specific resistivity of Hg is unusually high, 95.78 (in 10⁻⁸ Ωm), compared with that of Zn (5.8) or Cd (7.6).

Box 3 | **A head-on comparison of theory and experiment for the Au atom**

The ionization potential (IP) and electron affinity (EA) of the Au atom have been accurately measured by laser experiments. Pašteka et al.[70] reached theoretical meV accuracy by performing highly correlated calculations with a coupled-cluster method including up to pentuple excitations (DC-CCSDTQP) in a large basis (values are in eV)[70].

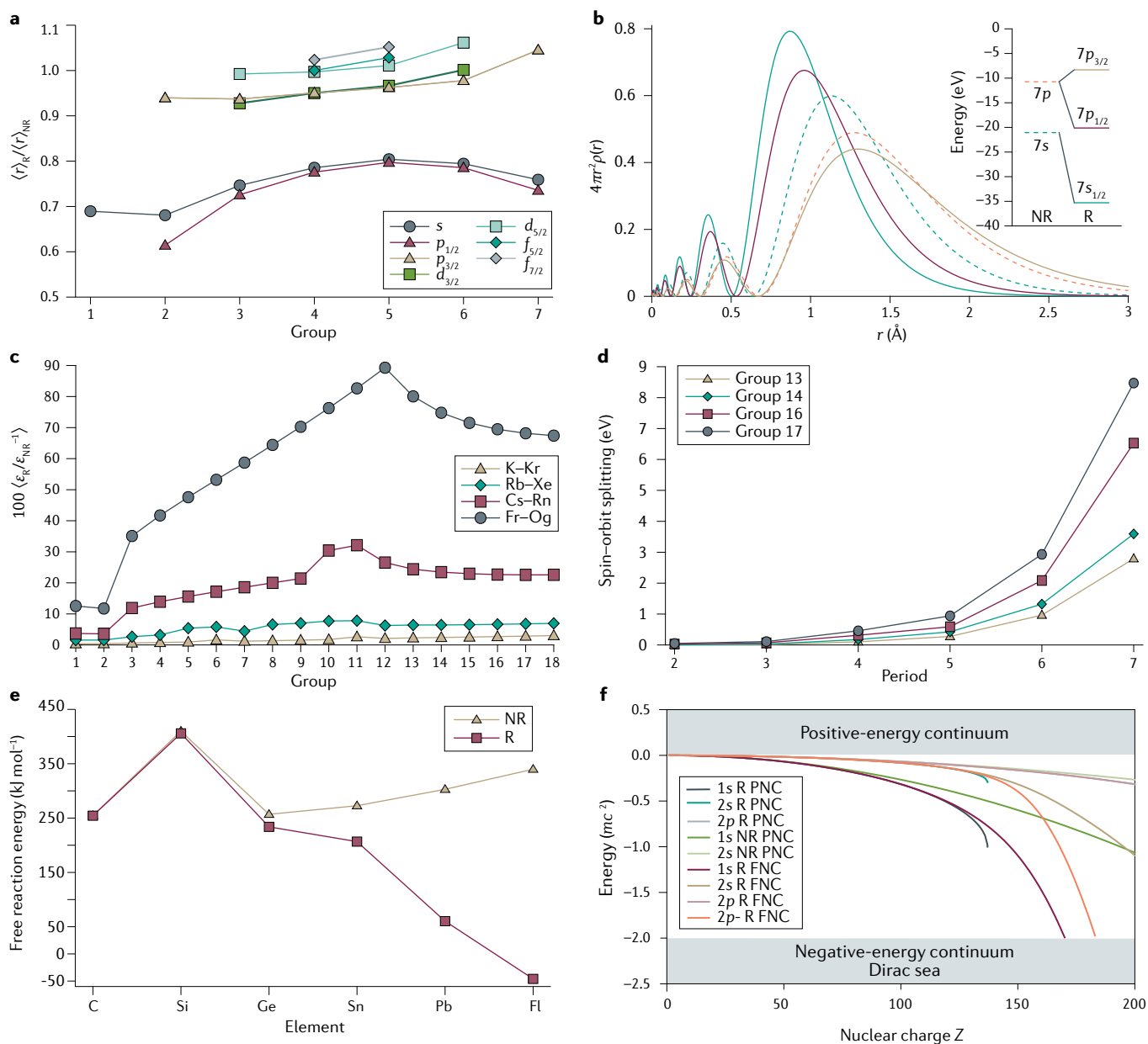| Method	IP		EA	
	Value	Error	Value	Error
DC-HF	7.6892	−1.5364	0.6690	−1.6396
DC-CCSDTQP	9.2701	0.0446	2.3278	0.0192
+Breit	9.2546	0.0290	2.3188	0.0102
+QED	9.2288	0.0032	2.3072	−0.0014
Exp.	9.2256		2.3086	

Fig. 4 | **Relativistic effects. a** | Ratio of the relativistic (R) to non-relativistic (NR) expectation values of average orbital radii, $\langle r \rangle$, for different Dirac–Hartree–Fock (nlj) orbitals in Og ($Z = 118$)[29,225]. **b** | NR and R radial densities, $4\pi r^2 \rho(r)$ for the valence $7s$ and $7p$ orbitals of Og. Corresponding orbital energies are given in the inset of the figure. **c** | Relativistic stabilization from R and NR orbital energies ε_R and ε_{NR}, respectively, of the ns shell for the elements K–Kr ($n = 4$), Rb–Xe ($n = 5$), Cs–Rn ($n = 6$) and Fr–Og ($n = 7$), showing the maximum of R effects in groups 11 and 12 of the periodic table of the elements. Redrawn from the data and configurations in REF.[29] and from numerical Hartree–Fock calculations (for Pd and Tc $4d^9 5s^1$ and $4d^5 5s^2$ configurations were chosen, respectively). See REFS[72,287] for details. **d** | Spin–orbit splitting for the group 13 (^{2}P), group 14 (^{3}P), group 16 (^{3}P) and group 17 (^{2}P) elements of the periodic table of the elements. Data taken from the National Institute of Standards and Technology (NIST)[285], for At and the superheavy elements from REFS[288,289] and from Dirac–Hartree–Fock–Breit calculations including quantum-electrodynamics effects[287]. **e** | R and NR free reaction energies for the decomposition $ECl_4 \rightarrow Cl_2 + ECl_2$ ($E = C$–Pb) at the density functional level of theory. Data are taken from REFS[18,116]. **f** | Diving of the $1s$ and $2s$ hydrogenic states into the negative-energy continuum for different levels of theory: NR Schrödinger equation with a point nuclear charge (PNC); Dirac–Coulomb equation (Dirac) with a PNC ending abruptly at Z_{crit}^{PNC}; Dirac–Coulomb equation with a finite nuclear charge distribution (FNC) using a two-parameter Fermi model[80]. $2p(j = 3/2)$ and $2p$-$(j = 1/2)$ are also shown. Note that the PNC and FNC $2p$ curves are indistinguishable on this plot. Part **b** is adapted from REF.[110], CC BY 4.0 (https://creativecommons.org/licenses/by/4.0/). Part **f** is adapted with permission from REF.[145], Elsevier.

An interesting property of Hg and its superheavy group member Cn is that they can both adopt the oxidation state +IV (REFS[83,94]) — HgF_4 has been identified not too long ago by Wang et al.[95]. The chemistry of Cn has recently been explored by using atom-at-a-time adsorption on Au surfaces, suggesting that this element is very volatile[96,97].

Spin–orbit effects in the p-block elements.
FIGURE 4d demonstrates the size of spin–orbit splitting in individual $l > 0$ shells for Og.

It diminishes for shells with higher angular quantum number l (as predicted by the Dirac equation) and is especially large for the lowest and highest principal quantum number n (FIG. 4a). Spin–orbit splittings for the group 13, 14, 16 and 17 elements follow

a $\sim Z^2$ behaviour (FIG. 4d) and, already for period 6, its effects become large enough to influence chemical bonding. However, during the formation of covalent bonds, spin–orbit effects can be substantially suppressed by the mixing of $p_{1/2}$ and $p_{3/2}$ orbitals to form σ or π bonds. For example, the combination of two $p_{1/2}$ orbitals at different atomic centres gives 1/3 of σ bonding and 2/3 of π^* antibonding or, switching sign, 2/3 of π bonding and 1/3 of σ^* antibonding. Additionally, combining two $p_{3/2}$ orbitals at different centres results in one π bond or a combination of 2/3 of π bonding and 1/3 of σ^* antibonding for $m_j = 3/2$ and 1/2, respectively[73,91,98]. This mixing also occurs in external fields; for example, spin–orbit effects can be suppressed in strong ligand fields during the formation of ionic bonds. Furthermore, electron density can move from the central atom to the electronegative ligand, thus diminishing spin–orbit effects, especially in the case of compounds in high oxidation states.

Spin–orbit effects are also the reason for a very small dissociation energy in Tl_2 (41 kJ mol^{-1})[99] and, consequently, a rather small cohesive energy for the bulk (182 kJ mol^{-1}) and low melting point (304 °C). This large spin–orbit destabilization is even more evident for the heaviest element dimer in group 13, Nh_2, in which the compact $7p_{1/2}$ shell and low population of the $7p_{3/2}$ orbital lead to a dissociation energy of only a few kJ mol^{-1}, in spite of the combination of two open-shell atoms[100,101]. Fl ($Z = 114$) has a closed spherical $7p_{1/2}^2$ shell well separated from the much higher lying $7p_{3/2}$ shell (FIG. 4d). Solid-state calculations indeed show that bulk Fl has a very small cohesive energy of 49 kJ mol^{-1} (down from 291 kJ mol^{-1} at the scalar relativistic level in which spin–orbit coupling is neglected) compared with Pb with 195 kJ mol^{-1} (REF.[102]). This is supported by atom-at-a-time adsorption experiments of Fl on a Au surface that indicate a higher inertness than its lighter group members, resulting in a high volatility[103,104]. According to these studies, Fl is the least reactive element in the group, but is still metallic in nature, and may be a liquid at room temperature[91].

It is well known that spin–orbit coupling is important for the correct interpretation of electronic spectra in atoms, molecules and the solid state. The photoelectron spectra of BiX_3 (X = Cl, Br, I) may serve as an interesting example[105]. In this case, the Bi–halogen σ bonding orbitals suffer from a relativistic rehybridization owing to spin–orbit coupling, and the energetic order of peaks is dominated by the central-atom spin–orbit splitting $\varepsilon(6p_{1/2}) < \varepsilon(6p_{3/2})$. In materials science, the Bi spin–orbit coupling helps to synthesize new high-pressure intermetallics[106].

As a last example, we mention the noble-gas element Og ($Z = 118$) (FIG. 4a,b), the last known p-block element and currently the heaviest element in the PTE. Here, the $^2P_{3/2}/^2P_{1/2}$ splitting in Og$^+$ is about 10 eV and larger than most bond-dissociation energies. In fact, Og is quite different to the lighter rare-gas atoms with an electron-localization function comparable to a Fermi gas[78] (both electron-localization and nuclear-localization functions are shown in FIG. 5). Og is predicted to be a solid under ambient conditions because of relativistic effects[107], exhibiting some unusual chemical and physical properties[107–110], such as a positive electron affinity of 0.056 eV (REF.[111]).

The inert-pair effect. The lowering of oxidation states in the 6p-block elements — such as Pb(II) compared with Sn(IV) — is linked to the so-called inert-pair effect, introduced by Sidgwick[112,113]. The inert-pair effect is the tendency of the two electrons in the outermost atomic s orbital to remain mostly unshared or localized in compounds of post-transition metals. Here, the increasing nuclear charge and relativistic effects down a group leads to the contraction of valence ns shell that results in a larger separation between the ns and np levels and to reduced mixing (hybridization) between the two, thus altering chemical bonding[114]. The relevant hybridization also accounts for the orbitals of the ligands[73]. Thus, the higher oxidation state becomes unfavourable, as seen, for example, in the group-13 and group-14 hydrides[115–117] or in the group-14 chlorides shown in FIG. 4e.

A striking example of the inert-pair effect is provided by the lead–acid battery, in which a great part of the voltage arises from relativistic effects[118]. The largest relativistic contribution comes from the high-energy compound Pb^{IV}O$_2$ in the lead–acid battery reaction: Pb(s) + PbO$_2$(s) + 2H$_2$SO$_4$(aq) → 2PbSO$_4$(s) + 2H$_2$O(l). Faraday's law, $\Delta G^0 = -RT \log(K) = -nFE^0_{cell}$ (in which G^0 is the standard Gibbs free energy, R is the gas constant, T is the temperature, K is the equilibrium constant, n is the number of electrons transferred, F is the Faraday constant and E^0_{cell} is the standard cell voltage), suggests that about 1.74 V of the total experimental cell voltage (2.107 V) is attributed to relativity.

Box 4 | Au is inherently relativistic

High-level calculations for the Au ionization potential E_{IP} and electron affinity E_{EA} (REF.[70]) show that electron correlation contributes 1.565 eV (17.0% of the experimental value) to E_{IP} and 1.650 eV (71.5%) to E_{EA} (at the Dirac–Coulomb–Breit level of theory). The same calculations show that relativistic effects contribute 2.140 eV (23.2%) to E_{IP} and 1.012 eV (43.8%) to E_{EA} (at the coupled-cluster level of theory). According to Mulliken's definition of the electronegativity χ_{Au}, the value $\chi = 0.187(E_{IP} + E_{EA})$ (E_{IP} and E_{EA} taken in units of eV) translates into a relativistic change[298] of $\Delta_R\chi = 0.59$. As a result, χ_{Au} is substantially increased, to ~2.4, and Au can be regarded both as a metal and as a pseudohalide. Therefore, relativistic effects influence the whole chemistry and physics of Au, leading to well-known anomalies in properties compared with those of Cu and Ag, as shown in the table below[79,299,300]. The most striking features to be highlighted are the yellow colour of bulk Au (REF.[301]), the catalytic activity and unusual structures of Au nanoclusters[302] and the high stability of high oxidation states, such as for the Au halides[303], and its associated role in homogeneous catalysis[304,305].

| Property	Cu	Ag	Au
Colour	Bronze	Silver	Yellow
Specific resistivity (10^{-8} Ωm)	1.72	1.62	2.4
Thermal conductivity (W cm^{-1} K^{-1})	3.85	4.18	3.1
Electronic heat capacity (10^{-4} J K^{-1} mol^{-1})	6.926	6.411	6.918
Melting point (°C)	1,083	961	1,064
Boiling point (°C)	2,567	2,212	3,080
Atomic volume (cm^3 mol^{-1})	7.12	10.28	10.21
Electronegativity	1.9	1.9	2.4
Polarizability (au)	46.5	55	36
Cohesive energy (kJ mol^{-1})	330	280	370
Desorption temperature CO on metal surface (K)	190–210	40–80	170–180
Common oxidation states	I, II	I	I, III
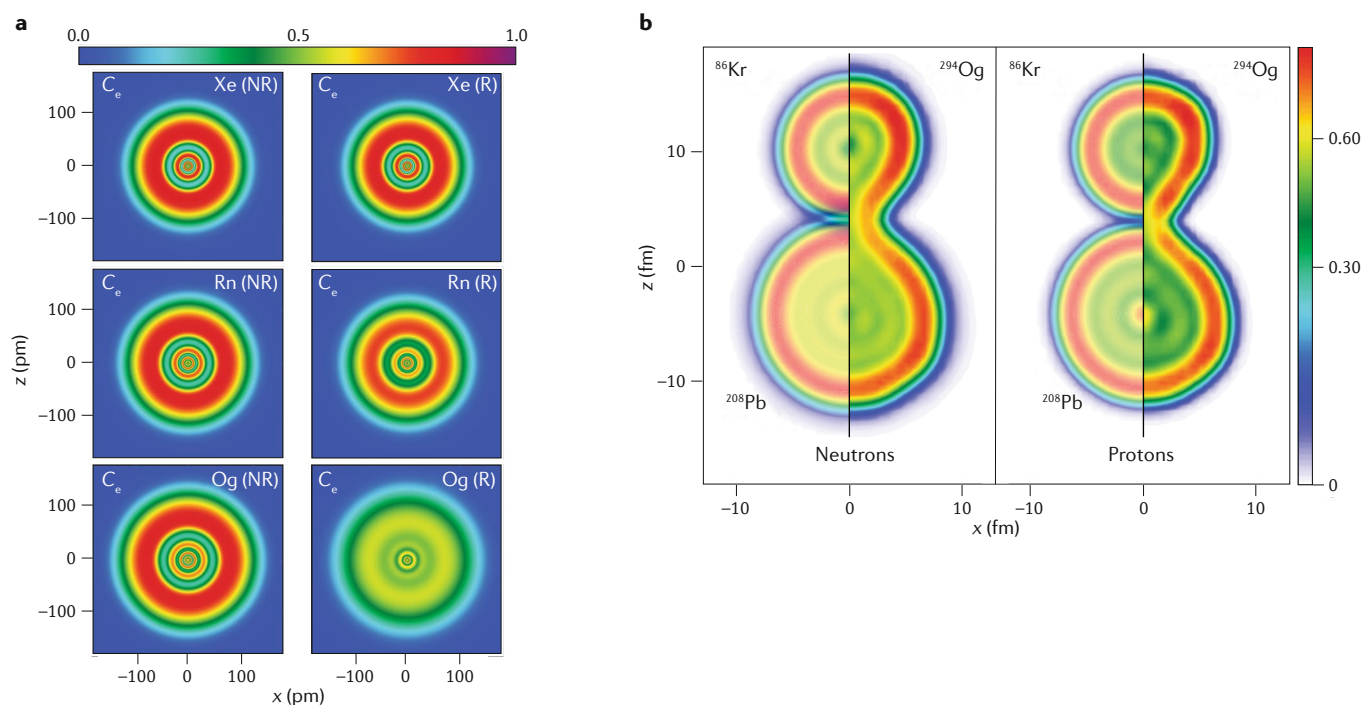
Fig. 5 | **Localization functions. a** | Electron-localization functions, C_e, from non-relativistic (NR) and Dirac–Hartree– Fock calculations (R) for the heavy rare-gas atoms Xe, Rn and Og showing the change in spatial localization of the electrons when moving to the heavier elements. **b** | Nucleon-localization function for a highly deformed configuration of $^{294}_{118}$Og for neutrons and protons. For comparison, localizations are shown for the prefragments $^{208}_{82}$Pb and $^{86}_{36}$Kr on the left side of each subplot, demonstrating the nuclear interactions in fission reactions. Part **a** is adapted with permission from REF.[78], American Physical Society. Part **b** is adapted with permission from REF.[261], American Physical Society.

For a more detailed discussion on the inert-pair effect, including a historical account, see REF.[114]. Further information on periodic trends in the main groups can be found in a recent paper by Frenking and colleagues[18].

The lanthanides. Lanthanides (Ln = La–Lu) are the elements in which the 4f shell is gradually filled. Typical Ln atom configurations are $4f^{G-3}5d^16s^2$ or $4f^{G-2}6s^2$ (G is the group number). Unlike the d-block elements, the compact 4f electrons are little involved in chemical bonding and act as 'spectators'. The 4f electrons can, thus, be treated (to a certain extent) as core-like. The formation of chemical bonds between Ln and other elements mainly involves Ln 6s and 5d[119,120]. Note that it is not important if the 5d shell is occupied in the atomic ground state, as long as it is energetically available. This is the main reason for the chemical similarity of the lanthanides — many of us know how hard it is to separate the different lanthanides.

The 4f electrons do, however, have a substantial influence on the physical properties of the lanthanide compounds because the 4f shell does not completely shield the nucleus. This leads to the so-called lanthanide contraction. With the increase

of the nuclear charge, the ionic radius of Ln^{3+} decreases from La to Lu, leading to progressively smaller bond distances in lanthanide compounds. The lanthanide contraction was introduced by Goldschmidt[121], who referred to both the contractions of radii in the series La–Lu, as well as the transition from pre-4f elements to post-4f elements (for example, Ag versus Au). Furthermore, the successive filling of the 4f shell has a significant influence on the 6s shell, for example, the relativistic stabilization of the 6s shell for La is 5.4% compared with 11.9% for Lu[29]. The core-like 4f states play a role in magnetic and optical properties of the lanthanides[122]. Lanthanides are mostly trivalent, except in cases like Eu(II) or Yb(II), in which half-filled or filled 4f shells favour divalency. Recently, low-valent compounds have been synthesized by Evans and colleagues[123].

The actinides. We analogously label actinides as An = Ac–Lr. The later actinides after Am are mostly trivalent and chemically similar to their Ln counterparts, creating problems in the chemical treatment of nuclear waste. In the range Th–Am, a rich hybridization and multiple bonding can occur, notably to N or O ligands, with the actinyl group being a prime example[124].

The main contributing An orbitals are 6d and 5f, with possible participation of the diffuse 7s and 7p, and the semicore 6p. It should be noted that the 5f shell has a larger radius than the 4f shell, both because it has a radial node and because it experiences an indirect relativistic destabilization. There has been a long-standing debate on the involvement of the 5f electrons in chemical bonding in certain compounds. For example, recent experimental and theoretical studies of Am–Cf consider systems with a half-filled 5f shell, such as Bk(IV) or Cf(V), and divalent An(II) compounds, in both non-aqueous and aqueous systems[125,126]. Both the An 6d and 5f orbitals are found to be involved. The debate on the role of 5f electrons focused mainly on the earlier actinide elements U and Np, which do not exhibit a proper actinide contraction[127].

As said, the insertion of the f elements into the periodic table and the resulting partial shielding of the nucleus have a profound influence on the chemistry of the post-f elements. Furthermore, relativistic effects increase the actinide contraction substantially[128]. Similar to the lanthanides, the relativistic stabilization of the 7s shell for Ac is 18.4% compared with 35.1% for Lr (FIG. 4c).

A more detailed discussion on shell-structure and relativistic effects for the lanthanides and actinides can be found in REFS[98,128,129]. For the discovery history of the elements 93–118, see REF.[130].

Beyond the known elements. How the PTE can be expanded beyond the currently known elements ($Z > 118$) has been discussed recently by Pyykkö[9,131]. The two elements that follow Og are the 8s elements below Fr and Ra, which have yet to be discovered. For details on current attempts carried out at the GSI (Germany), JINR (Russia) and RIKEN (Japan) laboratories to synthesize and detect superheavy elements beyond nuclear charge 118, the interested reader is referred to REFS[132–136]. So far, we have not discussed the chemistry of the alkali and alkaline-earth metals[18] because the properties of these elements are expected to become anomalous only for the heaviest two elements with $Z = 119$ and 120 (REFS[137–140]). After these two elements, one can nominally place the 18 5g elements 121–138 (REF.[9]). The atomic number at which the 5g shell begins to be populated is not clear, because electrons may alternatively fill 8s, $8p_{1/2}$, 7d and 6f orbitals. This problem has already been noted by Seaborg in the late 1960s[141]. According to one-valence-electron Dirac–Fock calculations, 5g becomes the lowest level from about $Z = 125$ (REF.[9]). This approximate beginning of some 5g atomic occupation has been known since the 1960s and used by Seaborg[141] to discuss the PTE. Because we count Th as an actinide even though its $7s^2 6d^2$ atomic ground state has no 5f electrons, we can welcome the elements 121–124 among the 5g elements.

Following the 5g elements, we have the $8p_{1/2}$ elements 139–140, then 6f elements 141–155 (note that we placed 15 elements here), succeeded by the 7d elements 156–164 (FIG. 1c). The density of electronic states in these elements becomes high. Therefore, in 1971, Fricke and colleagues suggested an alternative long-row model for their neutral-atom Dirac–Slater calculations, in which overlaps between different shell occupations are allowed[142]. They then placed the 9s elements at $Z = 165–166$, the $9p_{1/2}$ elements at 167–168 and, finally, the $8p_{3/2}$ elements at 169–172. The neutral-atom multi-configuration Dirac–Fock (MCDF) calculations of Indelicato and colleagues support the order arising from the Dirac–Slater calculations but exchange $8p_{3/2}$ with $9p_{1/2}$ (REF.[143]) and also add element 173. The chemistry of these elements still needs to be explored, including the correct assignment for the lowest (ground) state and low-lying

excited states and corresponding share of configurations. This requires high-level multi-reference theory, including QED[21,143]. This is basically unexplored territory and a major challenge for atomic-structure theory[38].

A first DFT attempt to study the chemistry of the 5g elements shows that the hypothetical octahedral hexafluorides, MF_6, of the elements with nuclear charge $Z = 125–129$ prefer occupied compact 5g (spectator) states similar to the 4f shell in the lanthanides[144]. As the 5g shell is even more compact than the Ln 4f shells[9], the 5g series would deserve the name of superlanthanides[8].

The critical nuclear charge. The PTE in FIG. 1c finishes with the last entry at $Z = 172$ (REFS[9,142]), while MCDF–QED calculations indicate element 173 to be the heaviest one[143]. It is often believed that the PTE (from an electronic point of view) cannot be expanded beyond a critical nuclear charge $Z_{crit} \approx 170$, a value above which atoms can no longer be described by the stationary Dirac–Coulomb equation[145]. According to the hydrogenic expression for the total energy arising from the Schrödinger equation, we have $E_n^{NR} = -Z^2/(2n^2)$ (in atomic units), that is, the energy decreases quadratically with nuclear charge (FIG. 4f). The corresponding Dirac equation for a point charge nucleus (point-like nucleus case, PNC) affords a different analytical expression of the energy:

$$E_{nj}/m_e c^2 = -1$$
$$+ \left(1 + \frac{(Z\alpha_{EM})^2}{[n-j-1/2 + \sqrt{(j+1/2)^2 - (Z\alpha_{EM})^2}]^2}\right)^{-1/2}$$

where m_e is the electron mass, c is the speed of light, α_{EM} the fine-structure (or electromagnetic coupling) constant and $j = l \pm 1/2$. FIGURE 4f shows that the non-relativistic energy starts to deviate substantially from the relativistic value at $Z \approx 60$ for the 1s orbital and $Z \approx 80$ for the 2s orbital. This deviation originates from the relativistic operators that act in the vicinity of the nuclei and from the s orbitals having higher electron density near the nucleus. However, the hydrogenic PNC–Dirac equation no longer has valid solutions for $Z > Z_{crit}^{PNC} = \alpha_{EM}^{-1}(j + 1/2)$, that is, for $Z > 137$ for s states, $Z > 274$ for $p_{3/2}$ and $d_{3/2}$ states and so on, as the total energy becomes imaginary. In mathematical terms, the Dirac operator is no longer self-adjoint; this happens even earlier for real eigenvalues

at $Z = 118$ (REFS[146,147]). The energy curves, therefore, end abruptly at $E_{crit}^{1s} = -m_e c^2$ and $E_{crit}^{2s} = -m_e c^2 (1 - 1/\sqrt{2})$. However, the introduction of a finite extension of the nuclear-charge (finite nucleus case, FNC) distribution removes this unphysical behaviour[148,149] (FIG. 4f). A comparison between the energy curves produced using the PNC and FNC models reveals that the PNC model becomes inaccurate for $Z > 120$ for the 1s state and $Z > 130$ for the 2s state. However, disaster strikes again when these states enter (dive into) the negative-energy continuum, the Dirac sea, at $Z_{crit}^{FNC} > 170$ for the 1s state and at much larger Z_{crit}^{FNC} value for the 2s state (note that the value of Z_{crit}^{FNC} depends on the nuclear-charge distribution used) (FIG. 4f). A remedy to this situation does not come easy and possible solutions have been proposed[150]. One possible explanation to this problem is that PTE does not end at some Z_{crit}. The description of multi-electron systems using the bare Dirac equation without the full QED framework in supercritical Coulomb fields provides an incomplete picture (note that, for multi-electron systems, the electron screening of the nucleus shifts Z_{crit}^{FNC} to higher values[145], but the diving is not avoided). In fact, as the 1s state at $Z > Z_{crit}^{FNC}$ is embedded in the Dirac continuum, the vacuum now becomes charged[150]. In a (multi-electron) system, the diving of an open shell will cause electron–positron pair creation, which should be observable in collisions of highly charged nuclei, resulting in a compound nucleus beyond the critical charge[151]. Besides, in this region of high nuclear charge, we expect the nuclear instability to be an 'earlier killer', as we see in the section Stability of superheavy elements[10].

Astrophysical nucleogenesis
Around 13.8 billion years ago, within approximately a second from the Big Bang, the most abundant elements in our universe were H ($_1^1$H and $_1^2$H) and He ($_2^4$He and $_2^3$He), with trace amounts of Li and some heavier elements also being present (FIG. 1d). All were formed from free neutrons and protons, radiative capture, neutrino interactions and subsequent nuclear fusion and decay reactions from the product isotopes. Under the influence of their mutual gravitational forces, the clouds of atomic H and He gas contracted, forming the first stars after 100 million years or so, leading to high temperatures and pressures in these population III stars, composed entirely of primordial gas. Through nuclear fusion in these young stars, heavier elements

(up to iron), including the isotopes essential to life ($_6^{12}$C and $_8^{16}$O), were formed and continue to form in existing stars. For elements lighter than iron, nuclear fusion releases energy when forming the most stable isotopes. For the heavier elements, instead, the nucleus is so tightly bound that nuclear fusion consumes energy. The fusion process of the star is, thus, halted when the silicon-burning phase has produced an iron core and, as a result, the star collapses under its gravitation force. Above a certain critical mass, when the star's core becomes as dense as an atomic nucleus, it rebounds explosively as a so-called supernova, releasing a flux of neutrons, protons and atoms into interstellar space, and, finally, a neutron star or black hole is formed[152].

Before we proceed with any further details, we point out that the efficient synthesis of C ($3\,_2^4$He $\rightarrow\,_6^{12}$C), O ($_6^{12}$C $+\,_2^4$He $\rightarrow\,_8^{16}$O) and other elements in stars requires a rather delicate tuning of two fundamental constants: the fine-structure constant α_{EM} and the strong-coupling constant α_S, which enter, amongst other coupling constants, the Standard Model in physics. Oberhummer and colleagues showed that, if α_S varies by 0.5% and α_{EM} by 4%, the stellar production of C or O will be reduced by a factor of 30–1,000 (REFS[153,154]). Furthermore, the neutron–proton mass difference $\Delta_{np}m = m_n - m_p$ is also sensitive to a change in α_{EM} or α_S. Borsanyi and colleagues showed that a value of $\Delta_{np}m < 0.45\,$MeV c^{-2} would cause H (proton) to undergo inverse β-decay (electron capture), resulting in predominant presence of neutrons in our universe[155]. A value of $\Delta_{np}m \sim 0.5\,$MeV c^{-2} would have resulted in the Big Bang nucleosynthesis producing much more $_2^4$He and far less H than it did in our universe. A considerably large value of $\Delta_{np}m = 1.3\,$MeV c^{-2} would have resulted in a faster β-decay for neutrons, leading to far fewer neutrons at the end of the Big Bang nucleosynthesis, making the burning of H in stars and the synthesis of the heavy elements difficult[155]. Thus, the existence of the elements in our universe is dictated by the fine-tuning of these fundamental constants, which we can measure very precisely but are yet to be understood[156]. The variation of fundamental constants in space–time might be linked to the existence of dark matter, and this is currently an active field of research in both physics and chemistry[157,158].

Returning to the astrophysical nucleosynthesis, a small percentage of the elements heavier than iron is produced by rapid proton capture (the *rp* process in binary star systems involving a neutron star where high temperatures above $10^9\,$K can be achieved to overcome the Coulomb barrier in nuclear reactions). This *rp* process produces proton-rich nuclei that can be identified on the right of the proton stability (drip) line shown in the (N, Z) (Segrè) chart[159–164] in FIG. 6a, reaching elements up to (perhaps) tellurium[165–167] (note that, at the proton and neutron drip lines, the nuclei are at the very edge of particle stability, such that they emit protons or neutrons, respectively, directly; drip-line isotopes provide very useful information for nuclear-structure theory). However, most of the heavy elements in the PTE are produced by neutron-capture processes, as first suggested by Gamow[168] in 1946 and by Alpher and Herman[169] in 1950. Neutron capture occurs on a timescale of roughly 1 s, which is three orders of magnitude smaller than the neutron half-life ($t_{1/2} = 883 \pm 7\,$s), which dictates its decay into a proton, an electron and an antineutrino[170–172]. In the nucleosynthesis process, neutrons are successively absorbed by a nucleus, creating isotopes on the left of the neutron drip lines. This is shown in the Segrè chart in FIG. 6a. At a certain mass number, the neutron-rich isotope will then β-decay to a more stable nucleus, with the nuclear charge increased from $Z \rightarrow Z+1$. This process repeats up to a nuclear charge Z that depends on the initial astrophysical conditions and the stability of the daughter nucleus at the end of the chain. FIGURE 6 contains a collection of graphs on nuclear stability and FIG. 6a shows such a possible path for the rapid neutron-capture process.

There are many possible astrophysical sites of neutron-rich matter (see discussion below) and many different processes and conditions[173,174]. However, for the synthesis of the heavy elements, we can identify four important types of neutron-capture process based on different astrophysical conditions: the rapid neutron capture (*r*-process) for number of neutrons $N_n > 10^{20}\,$cm^{-3} (for comparison, this is approximately equal to the number of ideal gas molecules under normal conditions)[175], the *n*-process for $N_n \approx 10^{18}\,$cm^{-3} (REF[176]), the intermediate neutron capture (*i*-process) for $N_n \approx 10^{15}\,$cm^{-3} (REFS[177,178]) and the slow neutron capture (the *s*-process) with $N_n = 10^6$–$10^{10}\,$cm^{-3} (REF[179]). These conditions define the different reaction paths and average time necessary before a neutron-rich isotope β-decays to a more stable nucleus with increased nuclear charge. Whereas *s*-capture produces nuclei near the valley of β-stability, for the *r*-process, the reaction path is shifted into the neutron-rich region of the nuclide chart because neutron-capture times in this case are much shorter than the average β-decay. Because of the loss of stability for elements heavier than Bi (the *s*-process terminates at $_{84}^{210}$Po), isotopes like U and Th can only be generated through an *r*-capture process. In these cases, the *s*-capture would be too slow and the intermediate nuclei decay before enough neutrons are captured to reach higher Z values[180,181] (BOX 5).

The two main neutron-capture processes, *r* and *s*, produce different isotope distributions; therefore, it is possible to identify the abundancy distribution for different heavy elements by their production type. For example, by comparing the isotopic abundance distribution with predictions from analytical models and nuclear-reaction networks coupled to stellar-evolution codes, it is predicted that about 51% of the heavy elements in the solar system originated through *s*-process nucleosynthesis, with the remaining 49% produced by other nucleosynthesis mechanisms, primarily the *r*-process[182]. An example of a comparison between experimental and predicted abundance distributions of elements that are produced by the *r*-capture and *s*-capture processes in the metal-poor star HD108317 is shown in FIG. 7a, where we see that the *s*-capture process terminates at $_{83}$Bi (blue line in BOX 5).

Abundance distributions using theoretical stellar evolutionary models were first predicted in the late 1950 to early 1960s by Burbidge, Clayton, Seeger and colleagues[165,183–185]. It was shown how, from the sequence of abundance distributions generated for specific numbers of neutrons per initial seed nucleus, one can estimate the superpositions of neutron exposures required to reproduce the experimentally observed abundance distributions of the isotopes produced through the *s*-process. An improved fit of simulation models to experimental data was later obtained by including more accurate evolution models and by integrating the full reaction network in the simulation[186–188]. Although the relative abundance distributions of the heavy elements in our universe obtained from numerical simulations nicely align with experimental results, it is very complicated to identify the astrophysical sites where the *s*-processes and *r*-processes take place. One relies on nucleosynthesis models that depend on nuclear-physics inputs and astrophysical conditions to get an idea of the origin of such processes. Distinguishing different astrophysical scenarios is challenging because the exact properties of
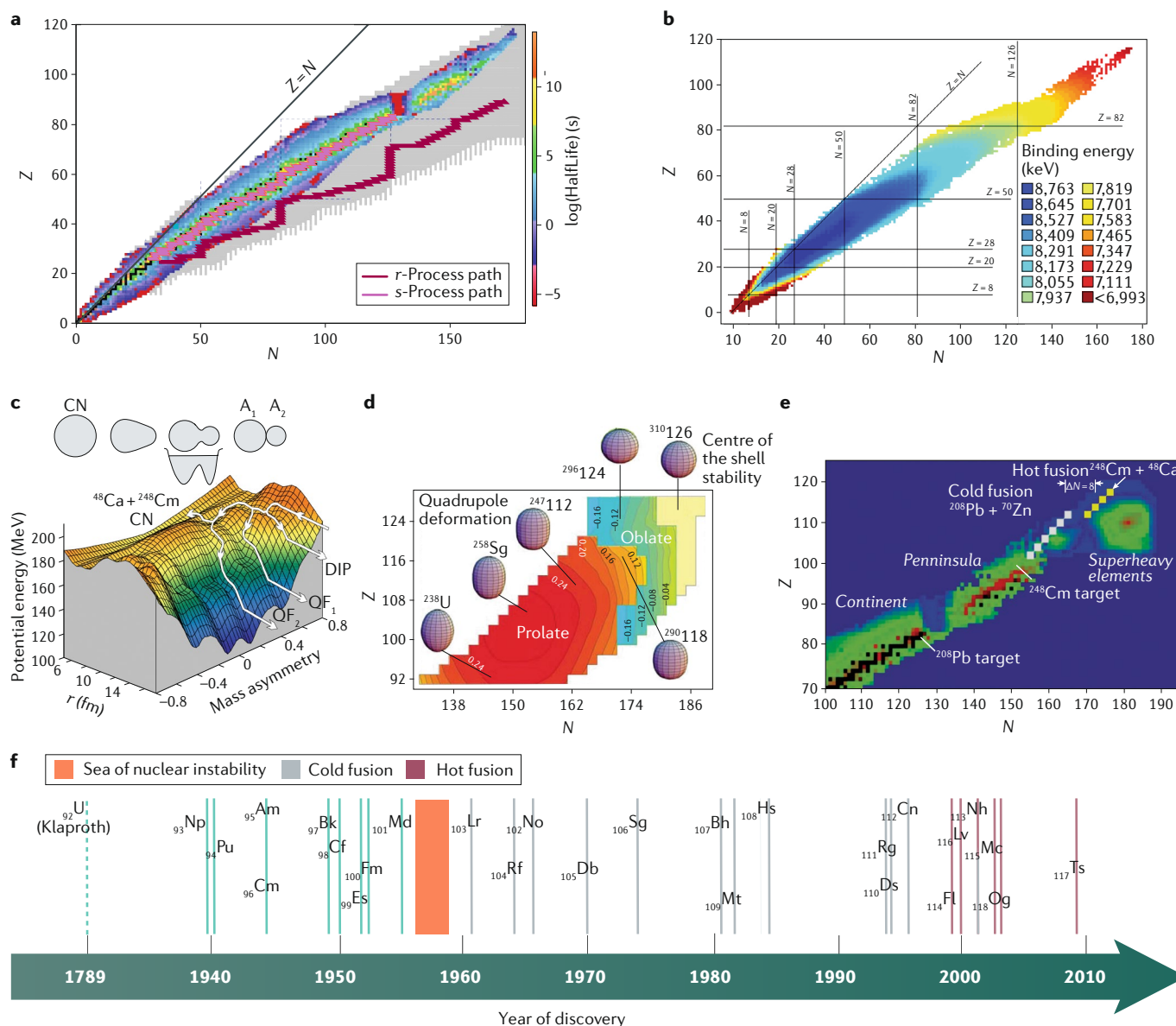
Fig. 6 | **Nuclear stability. a** | Chart of known and predicted (grey zone) nuclei coloured by their half-lives. The grey zone lies between the proton and neutron drip lines. Original graph provided by Brad Sherrill using half-lives from National Nuclear Data Center's NuDat 2 database. Added trajectories shown here for the rapid neutron capture, r-process, near the neutron drip line and the slow neutron capture, s-process, near the region of stability represent some of the many possible pathways (data from REF.[290]). **b** | Distribution of nuclides (isotopes) according to the binding energy per nucleon. The colour code indicates the different stabilities of the nuclides. Data obtained from the NuDat 2 database of the National Nuclear Data Center. **c** | Adiabatic potential energy of the $^{48}_{20}Ca + ^{248}_{96}Cm$ collision from a two-centre shell model. Different reaction channels, deep inelastic scattering (DIP), quasi-fission (QF) and fusion to the compound nucleus (CN), are shown schematically by the white arrows. The colour scale is chosen according to the potential-energy values on the hypersurface. **d** | Predicted ground-state mass quadrupole

deformation β_2 in the (N, Z) plane for even–even superheavy nuclei obtained from density functional theory calculations with a SLy4 nuclear energy density functional. The centre of the shell stability is predicted around $N = 184$, $Z = 126$. Prolate shapes are obtained for $\beta_2 > 0$, oblate shapes for $\beta_2 < 0$ and spherical shapes for $\beta_2 = 0$. **e** | Areas of stability and two examples of cold and hot fusion reactions and their α-decay products in the superheavy-element region. The red centre in the superheavy-element region around the magic number $Z = 114$ and $N = 184$ indicates enhanced shell stability. **f** | Timeline of discovery of the actinide and trans-actinide elements, including the original discovery of uranium by Klaproth in 1789. Part **a** image courtesy of B. Sherrill, Michigan State University, USA. Part **c** is adapted with permission from REF.[257], Elsevier. Part **d** is adapted from REF.[260], Springer Nature Limited. Part **e** is adapted with permission from REF.[291], Oganessian, Y. T. "Synthesis of the heaviest elements in 48Ca-induced reactions."; in: *Radiochim. Acta* **99**, de Gruyter, 2011, pp. 429–439.

the nuclear states of the isotopes involved in the capture process are difficult to obtain and the exact conditions of the ejecta are unknown. The easiest approach is to study events that happened shortly after the Big Bang because nearly all older stars contain

traces of products of the r-process. Another obstacle is the difficulty in obtaining information about exact stellar conditions. When nuclear excited states are thermally populated (which happens in stars but not in the laboratory), neutron capture can proceed

not only for nuclei in their ground states but also from nuclear excited states, and the reaction rates under stellar conditions are, thus, different from those measured in the laboratory. For these reasons, sites and mechanisms of neutron-capture production

---

Box 5 | The astrophysical *s*-neutron-capture and *r*-neutron-capture processes

Neutron capture and β-decay produce the heaviest elements in the periodic table. During the rapid neutron-capture process (*r*-process), which occurs in supernovae and neutron-star mergers, there are many possible reaction paths and the unstable nucleus captures another neutron before decaying. The *r*-process operates under conditions far from stability, closer to the neutron drip line. During the slow neutron-capture process (*s*-process), which occurs in stars (particularly, asymptotic giant branch stars), the unstable nucleus decays before capturing another neutron and the path is close to the valley of β-stability, as shown in the figure with known half-lives for the nuclear ground states included (data from REF.[165]).
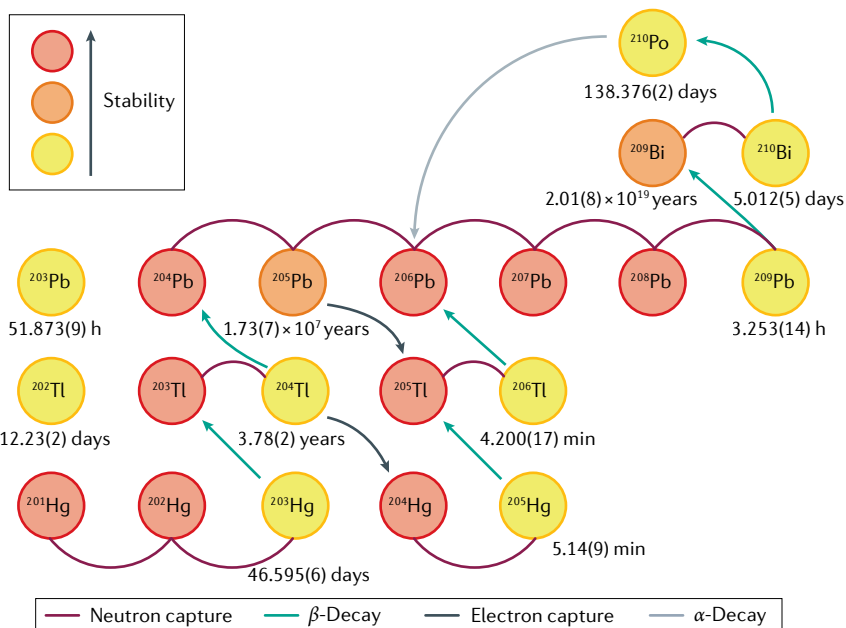
are still lacking substantial abundance observations to constrain proposed theoretical models.

First suggested by Ulrich[189], multiple neutron captures could take place in the He-rich layer of asymptotic giant branch (AGB) stars. During the late phase of the AGB, the thermal instability of the He burning shell leads to burning flashes of high amplitudes that establish convection zones that modify the distribution of He throughout the affected layers. As a result, H is reintroduced into hot layers, providing the flux of neutrons for the neutron-capture process[184,190,191]. Current models suggest the existence of two components to the *s*-process. The main *s*-component involves stars during their AGB phase (when they are in the mass range between 1 and 3 solar masses) that are responsible for the production of the isotopes in the mass region between Zr and Bi (mass number $A > 90$)[186,192]. The weak *s*-component occurs in massive AGB stars larger than 8 solar masses that are thought to be responsible for the production of elements between Fe and Zr ($60 < A < 90$)[193,194]. The existence of a third component was proposed after discovering that the main and weak *s*-components

do not fully reproduce the *s* abundances between Sr and Ba[195].

The *i*-process is thought to occur in carbon-enhanced metal-poor (CEMP) stars and the *n*-process in a supernova shock front traversing the He burning shell[176–178]. For the *r*-capture process, there are a number of possible astrophysical environments where it can occur. It was originally thought that *r*-capture occurs in supernovae[196]. Recent studies suggest neutron sources from kilonovae (merging neutron stars), because the *r*-process requires extreme conditions, although theoretical models do not exclude supernovae as sites of heavy *r*-processing[173,197–200]. The recently observed GW170817 neutron-star merger produced radiation across the electromagnetic spectrum consistent with the ejection of some hundredths of a solar mass of lanthanide-rich material[201,202]. This confirmed that heavy elements can be forged during such events, suggesting neutron-star mergers as the primary site for the *r*-process and possible production sites for the lighter actinides[203] and strontium[204]. The likely different astrophysical origins of the elements[165,205,206] are illustrated in the PTE in FIG. 1d. More experimental and theoretical

nuclear-structure data will be required in the near future to fully understand the various neutron-capture processes and the synthesis of the heavy elements.

Elements heavier than the U originating from neutron-capture processes have not been observed in larger amounts[207,208], despite a few searches and claims[209,210]. The main reason for this is that the fission barrier of the heavy nuclei produced during the *r*-capture process is lowered and, as a result, the heavy nuclei decay before neutron capture takes place. However, it is suggested that the production of heavy nuclei is enhanced if the *r*-process path proceeds closer to the neutron drip line. Petermann et al. performed fully dynamical network *r*-process calculations assuming an environment with a neutron-to-seed ratio large enough to produce superheavy nuclei with $Z \geq 104$ and $A \approx 300$ during the first seconds of the *r*-process[211] (FIG. 7b). However, the yields strongly depend on predicted nuclear data and astrophysical scenario, and the produced superheavy elements decay on timescales of seconds or minutes[212]. The lifetimes of superheavy nuclei are further discussed in detail in the next section.

Stability of superheavy elements

The heaviest naturally occurring elements of the PTE on our planet are U and trace amounts of ^{244}Pu found in the deep sea floor[213]. In fact, until 1943, only the elements up to Pu, which was produced by a deuteron bombardment of 238-U by Seaborg and colleages[214], were known (FIG. 1b). At that time, names like 'ultimium' or 'extremium' were considered for Pu because of the erroneous belief that this element might be the heaviest possible in the PTE[215–217].

In order to perform chemical experiments, a nucleus containing a given number of protons and neutrons needs to be sufficiently stable with respect to possible radioactive decay channels (from the confinement radius of an electron in an atom, $\sim 10^{-10}$ m, or a proton inside a nucleus, $\sim 10^{-15}$ m, and the corresponding masses, one can estimate the characteristic timescales for electronic and nuclear reactions using Heisenberg's formula, $\Delta E \Delta t > \hbar$, that are on the order of ~ 1 fs and 1 zs ($\sim 10^{-21}$ s), respectively). Current experimental approaches require a nuclear stability in the second range, which limits the study of the heaviest elements in the PTE, although this might be improved in the near future. In fact, at high nuclear charge, the PTE is limited not by the electronic but by the nuclear stability. Using a simple liquid-drop model, Bohr and Wheeler

established an upper limit of $Z^2/A = 47.8$ ($A - Z = N$), beyond which nuclei become unstable against the elongation of nuclear shape, resulting in spontaneous fission[218]. Using empirical (Z, A) relationships[219], this sets the upper limit of observable elements to $Z \sim 120$–130, after which the Coulomb repulsion between the protons inside a nucleus becomes too strong[220]. However, while these phenomenological theories based on the liquid-drop model offer great qualitative insight into nuclear properties, a proper treatment of nuclear-shell-structure effects is required to discuss the stability and possible decay channels for certain isotopes, for which the binding energy of the nucleus becomes an important property.

The total mass M of an atom in the PTE can be decomposed into $M(Z, N, N_e) = Zm_p + Nm_n + N_e m_e - B_{Z,N}/c^2 - B_e/c^2$, where $B_{Z,N}$ is the nuclear binding energy for a specific isotope and B_e is the total electronic binding energy ($B_e = -E_T$ for the total electronic energy) for N_e electrons ($N_e = Z$ for a neutral atom). The mass of a certain isotope can, nowadays, be determined to keV accuracy using a trap mass spectrometer or time-of-flight mass spectrometry[221–224]. The proton, neutron and electron masses are all accurately known to eV accuracy. The total electronic energy may be decomposed into $E_T = E_{NRHF} + \Delta E_{RHF} + \Delta E_{QED} + \Delta E_{cor}$, including the non-relativistic Hartree–Fock total energy (NRHF)[225], the relativistic energy correction at the Hartree–Fock level including the finite extension of the nucleus (RHF)[29], QED contributions[226,227] and electron-correlation effects to the many-electron QED Hamiltonian[228].

All these terms can be evaluated to eV (some of these to meV) accuracy, with the most problematic part being the electron-correlation contribution that amounts to ~0.4–0.5 eV per electron. This term can, however, be evaluated to an accuracy of 0.05 eV per electron. Hence, with future improvements in mass measurements, the remaining nuclear binding energy can be obtained to at least 1 keV accuracy. This level of accuracy is important for benchmarking nuclear-structure calculations. For example, nuclear DFT can currently reach an accuracy of only about 600 keV. Note that the electron-binding energy is not so small for the heavier elements compared with the nuclear part, because it increases with ~Z^2. For example, for $^{294}_{118}$Og, the relativistic binding energy is $B_e = 1.487$ MeV compared with the non-relativistic value of 1.260 MeV (REFS[10,78]).

A map of nuclear binding energies is shown in FIG. 6b (REF.[229]), in which we can observe the deviation of the nuclear binding energy from the $Z = N$ line. In other words, if Z increases, more neutrons are required to stabilize the nucleus against Coulomb repulsion. This, of course, explains the problem in the synthesis of superheavy elements with sufficiently long lifetimes from the beams and target isotopes available. Note that $B_{Z,N}$ varies in $[0, B_{max}]$, with the maximum binding energy per nucleon being that for ^{56}Fe, with $B_{max} = 8{,}792.23 \pm 0.03$ keV. There is no such upper limit in electronic-structure theory (at least for the non-relativistic case). Here, we point out another fundamental difference between electronic-structure and

nuclear-structure theory. The electronic binding energy for an N_e-electron system in the mean-field model follows approximately $B_e = \sum_{i=1}^{N_e} Z_{eff}^2(n_i, l_i, j_i)/n_i^2$ (see discussion above). This description separates energetically the core from the valence shells such that the chemistry of the elements in the PTE is dominated almost exclusively by the valence electrons (except for materials under high pressure[230,231]). This is the basis of the so-called effective core potential approximation well known to quantum chemists[232]. In nuclear-structure theory, there is no central field and we have a 'quantum liquid' of protons and neutrons. This, perhaps, is best demonstrated by the semi-empirical mass formula for nucleons[233], $B_{Z,N} = a_V A - a_S A^{2/3} - a_C Z(Z-1)A^{-1/3} - a_A A^{-1}(A - 2Z)^2 + \delta(A, Z)$, in which the dominant first (volume) term to the nucleon binding energy is linear in the number of nucleons A (the second term is the surface term, the third the Coulomb term, the forth the asymmetry term and the last one the empirical correction term).

It is beyond the scope of this Perspective to give an accurate account on current nuclear-structure theory (the reader is referred to a recent review article by Nazarewicz[234]). Instead, we point out some of the major differences between nuclear-structure theory and electronic-structure theory, which is more familiar to chemists, and the challenges that lie ahead in current nuclear-structure theory, especially for the treatment of superheavy elements. While the liquid-drop model is the earliest (collective) nuclear model introduced originally in the 1930s[218,235,236],
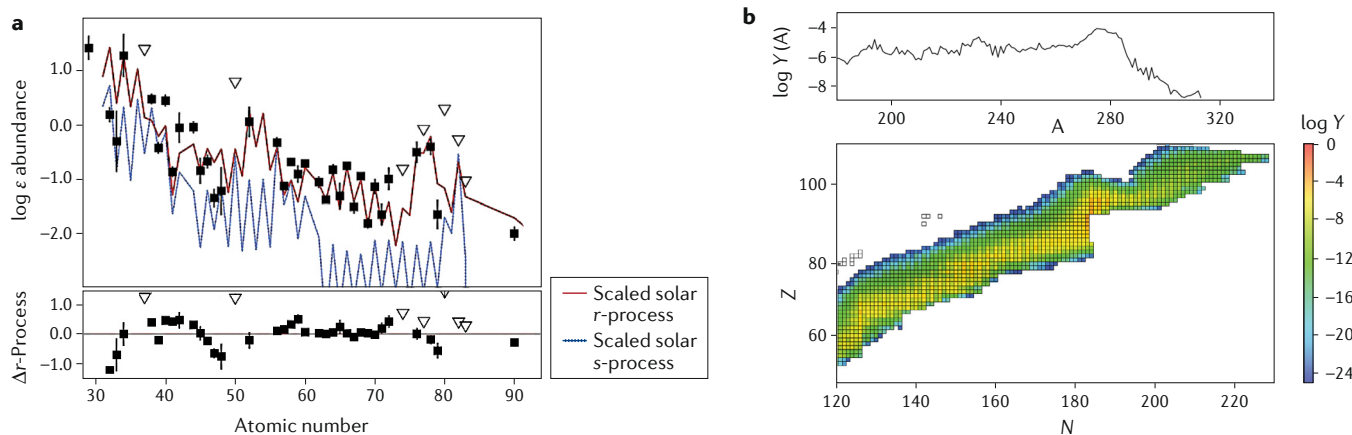

Fig. 7 | **Abundancies of elements. a** | Heavy-element abundance patterns in the metal-poor star HD108317. Black squares indicate detections from the Space Telescope Imaging Spectrograph on board the Hubble Space Telescope and open downward-pointing triangles indicate upper limits from predictions. The rapid neutron capture, *r*-process pattern, has been normalized to Eu, and the slow neutron capture, *s*-process pattern, has been normalized to Ba. The bottom panels show the abundance residuals with respect to the *r*-process pattern. **b** | Simulation under cold *r*-process conditions using the Thomas–Fermi model with Strutinski-integral method for fission barrier and mass predictions of the heaviest elements in the periodic table. The colour-coded abundances (right-hand side of the plot) are given at the point of neutron freeze-out, that is, when the ratio of neutrons to heavy nuclei has dropped down to 1 after $t = 0.7876$ s. Part **a** is adapted with permission from REF.[292], IOP. Part **b** is adapted from REF.[211], Springer Nature Limited.

Nuclear-structure theory is far more complicated than electronic-structure theory, owing to the strong and electromagnetic interactions of the neutrons and protons. The nuclear interaction is quite complex, involving many-body forces. However, nuclear-structure theory has developed rapidly over the past few decades owing to improved theoretical methods and para-meterizations, algorithms and computing power. In a fashion very similar to quantum chemistry, nuclear-structure theory ranges from more semi-empirical to more accurate methods (alternatively, wavefunction or density functional based). An overview of the different levels of approximations in use is given in the figure[234].
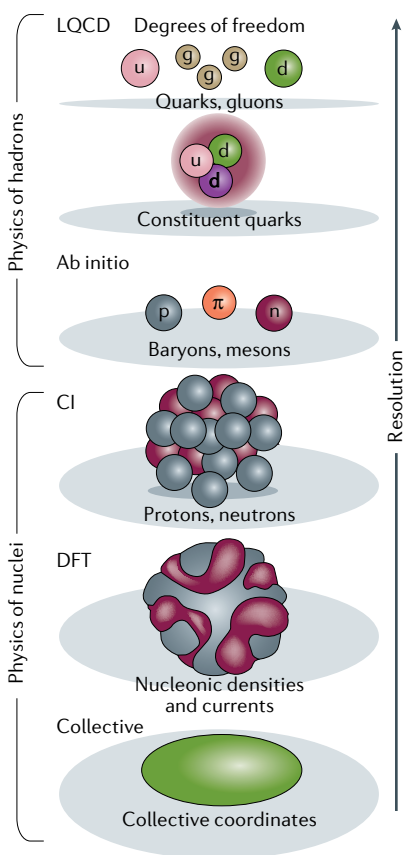
π, pion; CI, configuration interaction; DFT, density functional theory; d, down quark; g, gluon; LQCD, lattice quantum chromodynamics; n, neutron; p, proton; u, up quark. Figure reprinted with permission from REF.[306], AIP.

it was soon clear that, analogously to electronic structure theory, a nuclear shell model at the microscopic level was needed. In contrast to electronic-structure theory, in which the Hamiltonian is virtually known (for example, from the Schrödinger or Dirac–Coulomb equations with the additional corrections arising from QED and hyperfine interactions, containing

one-electron and two-electron operators only), the interactions between the nucleons are far more difficult to describe and are based on effective Hamiltonians or functionals. There is no a priori knowledge of the many-body forces between the nucleons and nuclear-structure theory becomes an effective-field theory. A most rigorous treatment at the quark level (lattice quantum chromodynamics) described by the Standard Model of physics is far too elaborate[237,238] for a complex many-nucleon system. Hence, one applies different levels of approximations, as outlined in BOX 6.

The effective nuclear-model Hamiltonians in wavefunction-based theories contain parameterized many-body forces, perhaps in some analogy to the treatment of long-range dispersive interactions between atoms or molecules for which, for example, a many-body decomposition of the total energy leads to very accurate results for properties of bulk rare gases[109,239,240]. Such model Hamiltonians can be treated at a high level of theory through configuration interaction or coupled-cluster theory[241–244] to account for nucleon correlation but still depend on the accurate description of the many-body forces. As nuclear matter is a strongly correlated quantum liquid, such calculations are expensive and currently applicable only to light and medium-sized nuclei[245,246]. This strong correlation also implies that the Hartree–Fock approximation is inadequate for a proper description of nuclear matter. For example, $^4_2$He coupled-cluster calculations for three-body Hamiltonians gave a binding energy of 28.24 MeV (REF.[246]) (extrapolated to the complete basis set limit) compared with 28.2957 MeV (7.0739 MeV per nucleon, see FIG. 6b) obtained from accurate mass measurements[247] and the mass formula shown above. The current accuracy in the most elaborate nuclear-structure calculations is on the order of 100 keV. Equation-of-motion–coupled-cluster (EOM–CC) theory, originally developed for quantum chemistry[248], can be used to calculate nuclear excited states. For example, $^{17}_8$O is a stable isotope with a (+5/2) ground state and a low-lying excited (+3/2) state at 0.870 MeV (REF.[249]) versus 1.219 MeV obtained using EOM–CCSD (which includes single and double excitations[250]).

Very similar to the situation in quantum-molecular dynamics, for nuclear-dynamic calculations, it remains a challenge to accurately predict nuclear reactions, radioactive-decay channels and corresponding lifetimes, such as nuclear

fission, α-decay and β-decay (we note that, while the free neutron decays with a half-life of 10.3 minutes, $^4_2$He is β-stable and no such decay is observed because of energy conservation[251]). For example, a comparison between calculated and spontaneous-fission half-lives using the (heavily parameterized) macroscopic–microscopic (mic–mac) model[252] including shell corrections for several superheavy elements showed deviations between theory and experiment within three orders of magnitude, with errors in binding energies in the MeV range[253]. Furthermore, tunnelling of particles through a potential barrier has an exponential dependence on the barrier height and width, which is well known in chemical dynamics (although, because of the collective dynamic behaviour of nucleons, the notion of a barrier becomes questionable)[254]. Nevertheless, it is difficult to accurately estimate decay properties, including lifetimes. Fortunately, there has been substantial development in nuclear-structure theory over the past 20 years that resulted in the improvement of both efficiency and accuracy for the computing of nuclear properties (BOX 6). This is especially the case for the nuclear self-consistent mean-field method, which has its roots in DFT[255]. In this approach, pairing correlation is taken into account using a pairing field obtained from Hartree–Fock–Bogoliubov calculations. For the nucleon potential, there are many approximations (such as Skyrme and Gogny) and parameterizations on nuclear data[255], very similar to quantum chemistry and the various density functionals. From such nuclear-structure calculations, one obtains proton and neutron densities (ρ_p and ρ_n, respectively), the corresponding nuclear deformations and shell energies. Spin–orbit interactions also need to be taken into account. Extensions beyond mean-field theory are again similar to those developed in quantum chemistry, like the random-phase approximation or multi-reference DFT. A complete overview on this subject has been given by Bender, Heenen and Reinhard[255]; therefore, we focus, for the remainder of this Perspective, on the mean-field results for the heaviest elements in the PTE.

For nuclear fusion or fission processes, the nuclear mass deformation (mainly quadrupolar and described by the parameter β_2)[256] is an important parameter that describes the elongation of nuclear shape and often serves as the main reaction coordinates. In fact, in nuclear physics, one obtains reaction profiles very similar

to chemical kinetics, except over different timescales (~1 zs) and energy scales (MeV). FIGURE 6c shows a total energy surface from nuclear-structure calculations for the nuclear decay of superheavy element 120, which is yet to be synthesized[257]. The picture clearly shows why there was such a long controversy in the past about the 'island of stability' (REF.[258]), that is, the compound nucleus lies very high on the energy surface in a rather shallow minimum with high probability for nuclear fission. According to modern theories, lifetimes of superheavy nuclei are fairly short because of fission and α-decay; hence, the notion of 'stable superheavy nuclei' is questionable[10,11]. From FIG. 6c, it is also clear that fusion cross sections are decreased substantially in the superheavy-element region, as many nuclear collisions will be unsuccessful and end in quasi-fission processes (quasi-fission is characterized by the formation of a composite system that does not reach the fully equilibrated compound nucleus) or in products from deep inelastic scattering. We note that the existence of transactinide nuclei completely relies on shell-structure stabilization[259]. Furthermore, above Fm, there are not enough neutrons inside the nucleus to reach the most stable predicted isotope, and there are currently no experiments on hand to add additional neutrons after the compound nucleus has formed (unlike in an astrophysical scenario). Hence, the superheavy elements are more on the proton-rich side of the nuclear landscape and they α-decay. Furthermore, many of the isotopes are not spherical but deformed[260] (FIG. 6d). Strong prolate deformations add to nuclear-fission instabilities. For example, nuclear-localization functions (similar to electron-localization functions) for nuclear fission (cluster decay) of $^{294}_{118}$Og are shown in FIG. 5b (REF.[261]). The nuclear-localization functions show the overlapping proton and neutron densities in a scission region, where the projectiles just touch, very similar to the overlap of electron densities in chemical reactions. Note that about 100 Og isotopes lie in between the proton and neutron drip lines, a territory that remains to be explored[10]. Another interesting feature in superheavy elements is that, because of Coulomb frustration, the protons are pushed out from the centre of the nucleus (semi-bubble structures), and the high proton and neutron densities of states leave the shells barely visible in nucleon-localization functions, in a manner very similar to the electronic case shown in FIG. 5a (REFS[11,78]). We note that high nuclear stability is obtained around proton and

neutron shell closures (so-called magic numbers 2, 8, 20, 28, 50 and 82 for closed proton or neutron shells are very similar to the magic numbers in electronic shell closures in atoms or clusters), where the nucleus becomes spherical. At higher magic numbers, one gets shell gaps at 126 and 184 for neutrons, and 114, 124 and 126 for protons[262,263]. It is worth noting that the notion of magic numbers in superheavy elements is being questioned because of high-level density of single-particle states and Coulomb frustration effects[10,11].

Nuclear-structure calculations are very important for the simulation of the astrophysical synthesis of the elements in the PTE and to predict the right beam and target conditions for the synthesis of new superheavy elements. In so-called cold-fusion reactions, the compound nucleus has a relatively low excitation energy, such that only a few neutrons are emitted and the fission process can be minimized. Targets used are $^{208}_{82}$Pb and $^{209}_{83}$Bi, and ^{278}Nh (half-life $t_{1/2} = 2.0^{+2.7}_{-0.7}$ ms) was the heaviest element synthesized at RIKEN laboratory in Japan through the ^{209}Bi(^{70}Zn,n)^{278}Nh cold-fusion reaction[134,264,265]. In hot-fusion experiments, the projectile nucleus is fixed to $^{48}_{20}$Ca and one requires rather heavy actinide targets with nuclei that are well deformed. Such combinations can lead to enhanced cross sections and enabled the synthesis of the elements beyond Nh up to Og (such as ^{249}Cf(^{48}Ca, $3n$)^{294}Og, $t_{1/2} = 0.69^{+0.64}_{-0.22}$ ms) by the JINR in Russia[266]. In the hot-fusion experiments, one ends up with a hot nucleus evaporating several neutrons, which is the reason that the hot-fusion reaction has been initially overlooked. Two examples of cold-fusion and hot-fusion reactions are shown in FIG. 6e, together with a colour-coded Segrè map of nuclear-decay lifetimes that shows enhanced stability at magic numbers $Z = 114$ and $N = 184$. The given lifetimes and the location of the maximum stability at $Z = 114$ has to be taken with care, though, as different nuclear models can predict lifetimes that differ by orders of magnitude, and it is currently not clear if the stability minimum lies at $Z = 120$, 122 or 126 (REF.[10]).

There are many reviews on the experimental synthesis of superheavy elements[10,130,267,268]. We summarize the history of discovery for the superheavy elements in FIG. 6f (REF.[130]); for a historical account and the many controversies surrounding the discovery of the superheavy elements, see REF.[269]. The progress towards the synthesis of an element with nuclear charge 119 is currently underway at RIKEN

laboratory in Japan and both the new JINR and GSI (Darmstadt) facilities will soon join the efforts in the synthesis of the elements beyond Og[282]. We can expect new elements, perhaps up to nuclear charge 126, in the next decade or so. For this reason, one has to move to heavier beams (^{50}Ti, ^{51}V, ^{54}Cr), because $_{98}$Cf is the heaviest target realistically available. It is clear that superheavy elements inhabit the remote corner of the nuclear landscape, but it is not yet clear what happens at much higher nuclear charge. Reliable predictions of lifetimes for different decay channels beyond $Z = 118$ are currently not available, and it is not known if exotic topologies of nuclear density can produce long-lived isotopes. Also, the limits of nuclear mass and charge are currently not known and we expect that nuclear stability will be the limiting factor well below the electronic critical nuclear charge Z^{FNC}_{crit} (REFS[10,11]). The binding energies in FIG. 6b suggest that the PTE is not infinite; nevertheless, this unknown territory needs to be explored in terms of both nuclear-structure theory and quantum chemistry.

Conclusions

The PTE has its solid foundation in quantum theory and is firmly based on both the Pauli and Aufbau principles, giving rise to chemical similarities within a specific group. Similarities between elements in the PTE depend on the accessibility of valence electrons for overlap and charge transfer, as well as on electron-correlation and relativistic effects. Subtle shell-structure effects cause irregularities and anomalies in the chemical and physical behaviour of the elements within a specific group. Fuzzy concepts like chemical similarity[270] often lead to unnecessary disputes concerning the PTE. The ambiguity of clearly assigning a specific element into the right place of the PTE, as for the lanthanides and actinides, shows the limitation of such concepts or approximations[271–274] but, in our opinion, should not be over-interpreted, as it is sometimes done. We should be reminded that electron configurations arising from the Aufbau principle originate from a mean-field (one-particle) approximation, which can fail for strongly correlated (highly multi-configurational) systems, especially when the density of states becomes large (remember the different electron configurations and dense spectra within the group 10 atoms), as is the case for the transactinides and into the superheavy-element region of the PTE. To cite Werner Kutzelnigg: "… one would

like to learn more is whether the periodic system has a chance to survive in the realm of superheavy elements"[275]. Thus, the PTE as suggested recently by one of the authors (FIG. 1c) should be seen as a first good approximation, and future theoretical investigations will offer us more insight on the electronic structure of the elements up to the critical nuclear charge Z_{crit}. Beyond Z_{crit}, we need to take into account the charged vacuum, which will make a multi-electron treatment, including electron correlation, a challenge for future theoretical studies. But this is not the end of the PTE.

Relativistic effects lead to interesting anomalies within the PTE, even for atoms with the same electron configuration. These effects are enhanced for the elements that exhibit subtle shell-structure effects, such as the group 11 and group 12 elements Au and Hg and their heavier analogues. However, we would not place these elements anywhere else in the PTE because of their dissimilarities to their lighter congeners. Furthermore, spin–orbit coupling in the p-block of the PTE has significant influence on their chemical and physical properties. As a curiosity, the element Og can be seen as almost Fermi-like electron gas and is predicted to be a solid at room temperature. Relativistic effects in the region beyond the known elements remain mostly unexplored and we can expect the unexpected here[81,276].

Developments in nuclear-structure theory and experimental measurements over the past few decades have provided us with very useful data for the prediction of astrophysical-synthesis processes (see, for example, the most recent work on the fate of intermediate-mass stars by Kirsebom and colleagues[277]) and for many other applications in nuclear physics such as beam–target design in the synthesis of superheavy elements. Superheavy elements have possibly been synthesized in r-processes originating from neutron-star mergers or supernovae but have long since decayed and are unlikely to be found on our planet. Over the past 20 years, we saw the addition of nine new elements in the PTE, and experiments to obtain elements beyond nuclear charge $Z = 118$ are currently underway. The PTE is finite because of nuclear stability and it will be an exciting time to explore the remote corner of the PTE.

The PTE is intrinsically linked to fundamental physics. From a fundamental-physics point of view, all four fundamental forces are important for the distribution of the elements in our universe and on our planet Earth. Without the electromagnetic force, there would be no atoms and without the strong force, no nuclei, including the proton and neutron, nor without the weak force any production of the heavy elements through β-decay. Finally, without the gravitational force, no stars would form, and no important elements like carbon and oxygen formed nor accumulated on Earth or other planets. Moreover, the efficient astrophysical-nucleosynthesis process depends on the fundamental constants with a rather narrow range of permitted values to sustain the existence of the elements in the PTE.

We finish with two quotes, the first by Primo Levi (*The Periodic Table*)[278]: "Conquering matter is to understand it, and understanding matter is necessary to understanding the Universe and ourselves: and that therefore Mendeleev's Periodic Table, which just during those weeks we were learning to unravel, was poetry." The second by John Emsley (*Nature's Building Blocks: An A-Z Guide to the Elements*)[279]: "As long as chemistry is studied, there will be a periodic table. And even if someday we communicate with another part of the Universe, we can be sure that one thing both cultures will have in common is an ordered system of the elements that will be instantly recognizable by both intelligent life forms."

Peter Schwerdtfeger [1,2✉], *Odile R. Smits*[1✉] *and Pekka Pyykkö* [3✉]

¹Centre for Theoretical Chemistry and Physics, New Zealand Institute for Advanced Study and the Institute of Natural and Mathematical Sciences, Massey University Auckland, Auckland, New Zealand.

²Centre for Advanced Study (CAS) at the Norwegian Academy of Science and Letters, Oslo, Norway.

³Department of Chemistry, University of Helsinki, Helsinki, Finland.

✉e-mail: *p.a.schwerdtfeger@massey.ac.nz; smits.odile.rosette@gmail.com; pekka.pyykko@helsinki.fi*

1. Mendelejew, D. Über die Beziehungen der Eigenschaften zu den Atomgewichten der Elemente. *Zeit. Chem.* **12**, 405–406 (1869).
2. Van Spronsen, J. W. *The Periodic System of Chemical Elements: A History of the First Hundred Years* (Elsevier, 1969).
3. Kaji, M. D. I. Mendeleev's concept of chemical elements and the principles of chemistry. *Bull. Hist. Chem.* **27**, 4–16 (2002).
4. Scerri, E. R. *The Periodic Table: Its Story and Its Significance* (Oxford Univ. Press, 2007).
5. Gordin, M. D. *A Well-Ordered Thing: Dmitrii Mendeleev and the Shadow of the Periodic Table* (Princeton Univ. Press, 2018).
6. Pushcharovsky, D. Dmitry I. Mendeleev and his time. *Substantia* **3**, 119–129 (2019).
7. Shaik, S., Cremades, E. & Alvarez, S. The periodic-table—a universal icon: its birth 150 years ago, and its popularization through literature art and music. *Angew. Chem. Int. Ed.* **58**, 13194–13206 (2019).
8. Pyykkö, P. An essay on periodic tables. *Pure Appl. Chem.* **91**, 1959–1967 (2019).
9. Pyykkö, P. A suggested periodic table up to Z ≤ 172, based on Dirac–Fock calculations on atoms and ions. *Phys. Chem. Chem. Phys.* **13**, 161–168 (2011).
10. Giuliani, S. A. et al. *Colloquium*: superheavy elements: oganesson and beyond. *Rev. Mod. Phys.* **91**, 011001 (2019).
11. Nazarewicz, W. The limits of nuclear mass and charge. *Nat. Phys.* **14**, 537–541 (2018).
12. Pauling, L. *The Nature of the Chemical Bond* (Cornell Univ. Press, 1960).
13. Ruedenberg, K. The physical nature of the chemical bond. *Rev. Mod. Phys.* **34**, 326 (1962).
14. Frenking, G. & Shaik, S. *The Chemical Bond* (Wiley, 2014).
15. Bacskay, G. B., Nordholm, S. & Ruedenberg, K. The virial theorem and covalent bonding. *J. Phys. Chem. A* **122**, 7880–7893 (2018).
16. Zhao, L.-L., Schwarz, W. H. E. & Frenking, G. The Lewis electron-pair bonding model: the physical background one century later. *Nat. Revs. Chem.* **3**, 35–47 (2019).
17. Pauli, W. The connection between spin and statistics. *Phys. Rev.* **58**, 716–722 (1940).
18. Zhao, L., Pan, S., Holzmann, N., Schwerdtfeger, P. & Frenking, G. Chemical bonding and bonding models of main-group compounds. *Chem. Rev.* **119**, 8781–8845 (2019).
19. Goidenko, I. A. QED corrections for the valence electron in the heavy and superheavy metal atoms from the 11 and 12 groups. *Eur. Phys. J. D* **55**, 35–42 (2009).
20. Goidenko, I., Labzowsky, L., Eliav, E., Kaldor, U. & Pyykkö, P. QED corrections to the binding energy of the eka-radon (Z = 118) negative ion. *Phys. Rev. A* **67**, 020102 (2003).
21. Thierfelder, C. & Schwerdtfeger, P. Quantum electrodynamic corrections for the valence shell in heavy many-electron atoms. *Phys. Rev. A* **82**, 062503 (2010).
22. Slater, J. C. Atomic shielding constants. *Phys. Rev.* **36**, 57–64 (1930).
23. Zener, C. Analytic atomic wave functions. *Phys. Rev.* **36**, 51–56 (1930).
24. Fermi, E. Anomalous groups in the periodic system of elements. *Nature* **121**, 502 (1928).
25. Ivanenko, D. D. & Larin, S. *Theory of the Periodic System of the Elements* Vol. 2 (U.S. Atomic Energy Commission, Technical Information Service, 1953).
26. Landau, L. D. & Lifshitz, E. M. *Quantum Mechanics: Non-Relativistic Theory* 2nd edn Vol. 3 (Pergamon, 1965).
27. Essén, H. Periodic table of the elements and the Thomas–Fermi atom. *Int. J. Quant. Chem.* **21**, 717–726 (1982).
28. Hartree, D. R. Variation of atomic wave functions with atomic number. *Rev. Mod. Phys.* **30**, 63–68 (1958).
29. Desclaux, J. P. Relativistic Dirac-Fock expectation values for atoms with Z = 1 to Z = 120. *At. Data Nucl. Data Tables* **12**, 311–406 (1973).
30. Pyykkö, P. The physics behind chemistry and the periodic table. *Chem. Rev.* **112**, 371–384 (2012).
31. Mazurs, E. G. *Graphic Representations of the Periodic System During One Hundred Years* (Univ. Alabama Press, 1974).
32. Bensaude-Vincent, B. in *Tools and Modes of Representation in the Laboratory Sciences* (ed. Klein, U.) 133–161 (Springer, 2001).
33. Goudsmit, S. A. & Richards, P. I. The order of electron shells in ionized atoms. *Proc. Natl Acad. Sci. USA* **51**, 664–671 (1964).
34. Madelung, E. *Die Mathematischen Hilfsmittel des Physikers* 3rd edn (Springer, 1936).
35. Janet, C. *Concordance de l'Arrangement Quantique, de Base, des Électrons Planétaires, des Atomes, avec la Classification Scalariforme, Hélicoïdale, des Élements Chimiques* (Beauvais Imprimerie Départementale de l'Oise, 1930).
36. Sommerfeld, A. Electronic structure of the atom and the quantum-theory. *Mem. Proc. Manchester Lit. Phil. Soc.* **70**, 141–151 (1925).
37. Allen, L. C. & Knight, E. T. The Löwdin challenge: origin of the n + ℓ, n (Madelung) rule for filling the orbital configurations of the periodic table. *Int. J. Quantum Chem.* **90**, 80–88 (2002).
38. Nefedov, V. I., Trzhaskovskaya, M. B. & Yarzhemskii, V. G. Electronic configurations and the periodic table for superheavy elements. *Dokl. Phys. Chem.* **408**, 149–151 (2006).
39. Laing, M. A revised periodic table: with the lanthanides repositioned. *Found. Chem.* **7**, 203 (2005).
40. Scerri, E. R. & Parsons, W. *Mendeleev to Oganesson: A Multidisciplinary Perspective on the Periodic Table* (eds Scerri, E. & Restrepo, G.) 140–151 (Oxford Univ. Press, 2018).
41. Xu, W.-H. & Pyykkö, P. Is the chemistry of lawrencium peculiar? *Phys. Chem. Chem. Phys.* **18**, 17351–17355 (2016).

42. Steinhauser, G. Wohin mit dem f-block? *Nachr. Chem.* **67**, 8–11 (2019).
43. Eichler, R. The periodic table–an experimenter's guide to transactinide chemistry. *Radiochim. Acta* **107**, 865–877 (2019).
44. Cao, C.-S., Hu, H.-S., Li, J. & Schwarz, W. H. E. Physical origin of chemical periodicities in the system of elements. *Pure. Appl. Chem.* **91**, 1969–1999 (2019).
45. Grupen, C. *Astroparticle Physics* 339–355 (Springer, 2020).
46. Kolar, M., Kubar, T. & Hobza, P. On the role of London dispersion forces in biomolecular structure determination. *J. Phys. Chem. B* **115**, 8038–8046 (2011).
47. Moreno, D. et al. Re-examination of the C_6Li_6 structure: to be, or not to be symmetric. *Chem. Eur. J.* **19**, 12668–12672 (2013).
48. Drozdov, A., Eremets, M. I., Troyan, I. A., Ksenofontov, V. & Shylin, S. I. Conventional superconductivity at 203 kelvin at high pressures in the sulfur hydride system. *Nature* **525**, 73–76 (2015).
49. Somayazulu, M. et al. Evidence for superconductivity above 260 K in lanthanum superhydride at megabar pressures. *Phys. Rev. Lett.* **122**, 027001 (2019).
50. Drozdov, A. P. et al. Superconductivity at 250 K in lanthanum hydride under high pressures. *Nature* **569**, 528–531 (2019).
51. Loubeyre, P., Occelli, F. & Dumas, P. Synchrotron infrared spectroscopic evidence of the probable transition to metal hydrogen. *Nature* **577**, 631–635 (2020).
52. Drake, G. W. F. & Martin, W. C. Ionization energies and quantum electrodynamic effects in the lower 1sns and 1snp levels of neutral helium (4He I). *Can. J. Phys.* **76**, 679–698 (1998).
53. Hotokka, M., Kindstedt, T., Pyykkö, P. & Roos, B. O. On bonding in transition-metal helide ions. *Mol. Phys.* **52**, 23–32 (1984).
54. Wesendrup, R., Pernpointner, M. & Schwerdtfeger, P. Coulomb-stable triply charged diatomic: HeY^{3+}. *Phys. Rev. A* **60**, R3347–R3349 (1999).
55. Wright, T. G., Lee, E. P. F., Hotokka, M. & Pyykkö, P. Al^{3+}-He: stability and spectroscopy. *Chem. Phys. Lett.* **392**, 281–283 (2004).
56. Dong, X. et al. A stable compound of helium and sodium at high pressure. *Nat. Chem.* **9**, 440–445 (2017).
57. Pyykkö, P. Dirac-Fock one-centre calculations part 8. The 1σ states of ScH, YH, LaH, AcH, TmH, LuH and LrH. *Phys. Scr.* **20**, 647–651 (1979).
58. Shchukarev, S. A. in *Periodicheskij Zakon i Stroenie Atoma* (ed. Levinski, Y. V.) (Atomizdat, 1971).
59. Imyanitov, N. S. Does the period table appear doubled? two variants of division of elements into two subsets. internal and secondary periodicity. *Found. Chem.* **21**, 255–284 (2019).
60. Trinquier, G., Malrieu, J.-P. & Daudey, J.-P. Ab initio study of the regular polyhedral molecules N_4, P_4, As_4, N_8, P_8 and As_8. *Chem. Phys. Lett.* **80**, 552–557 (1981).
61. Kutzelnigg, W. Chemical bonding in higher main group elements. *Angew. Chem. Int. Ed.* **23**, 272–295 (1984).
62. Düllmann, C. E. et al. Chemical investigation of hassium (element 108). *Nature* **418**, 859–862 (2002).
63. Lu, J.-B. et al. Experimental and theoretical identification of the Fe(vii) oxidation state in FeO_4^-. *Phys. Chem. Chem. Phys.* **18**, 31125–31131 (2016).
64. Autschbach, J., Siekierski, S., Seth, M., Schwerdtfeger, P. & Schwarz, W. H. E. Dependence of relativistic effects on electronic configuration in the neutral atoms of d- and f-block elements. *J. Comput. Chem.* **23**, 804–813 (2002).
65. Mann, J. B., Meek, T. L., Knight, E. T., Capitani, J. F. & Allen, L. C. Configuration energies of the d-block elements. *J. Am. Chem. Soc.* **122**, 5132–5137 (2000).
66. Allen, L. C. Extension and completion of the periodic table. *J. Am. Chem. Soc.* **114**, 1510–1511 (1992).
67. Nyholm, R. S. Electron configuration and structure of transition-metal complexes. Tilden Lecture. *Proc. Chem. Soc.* **1961**, 273–298 (1961).
68. Kaupp, M. The role of radial nodes of atomic orbitals for chemical bonding and the periodic table. *J. Comput. Chem.* **28**, 320–325 (2007).
69. Newell, D. B. et al. The CODATA 2017 values of h, e, k, and NA for the revision of the SI. *Metrologia* **55**, L13 (2018).
70. Paŝteka, L. F., Eliav, E., Borschevsky, A., Kaldor, U. & Schwerdtfeger, P. Relativistic coupled cluster calculations with variational quantum electrodynamics resolve the discrepancy between experiment and

theory concerning the electron affinity and ionization potential of gold. *Phys. Rev. Lett.* **118**, 023002 (2017).
71. Rose, S. J., Grant, I. P. & Pyper, N. C. The direct and indirect effects in the relativistic modification of atomic valence orbitals. *J. Phys. B* **11**, 1171–1176 (1978).
72. Pyykkö, P. & Desclaux, J. P. Relativity and the periodic system of elements. *Acc. Chem. Res.* **12**, 276–281 (1979).
73. Pyykkö, P. Relativistic effects in structural chemistry. *Chem. Rev.* **88**, 563–594 (1988).
74. Pyykkö, P. Relativistic effects in chemistry: more common than you thought. *Annu. Rev. Phys. Chem.* **63**, 45–64 (2012).
75. Schwarz, W. H. E., van Wezenbeek, E. M., Baerends, E. J. & Snijders, J. G. The origin of relativistic effects of atomic orbitals. *J. Phys. B* **22**, 1515–1530 (1989).
76. Dehmer, J. L. Phase-amplitude method in atomic physics. II. Z dependence of spin-orbit coupling. *Phys. Rev. A* **7**, 4–9 (1973).
77. Mayers, D. F. Relativistic self-consistent field calculation for mercury. *Proc. R. Soc. A* **241**, 93–109 (1957).
78. Jerabek, P., Schuetrumpf, B., Schwerdtfeger, P. & Nazarewicz, W. Electron and nucleon localization functions of oganesson: approaching the Thomas-Fermi limit. *Phys. Rev. Lett.* **120**, 053001 (2018).
79. Schwerdtfeger, P. & Lein, M. in *Gold Chemistry: Applications and Future Directions in the Life Sciences* (ed. Mohr, F.) 183–247 (Wiley, 2009).
80. Dyall, K., Grant, I., Johnson, C., Parpia, F. & Plummer, E. GRASP: a general-purpose relativistic atomic structure program. *Comput. Phys. Commun.* **55**, 425–456 (1989).
81. Türler, A. & Pershina, V. Advances in the production and chemistry of the heaviest elements. *Chem. Rev.* **113**, 1237–1312 (2013).
82. Eliav, E., Kaldor, U., Schwerdtfeger, P., Hess, B. A. & Ishikawa, Y. Ground state electron configuration of element 111. *Phys. Rev. Lett.* **73**, 3203–3206 (1994).
83. Seth, M., Schwerdtfeger, P. & Dolg, M. The chemistry of the superheavy elements. I. Pseudopotentials for 111 and 112 and relativistic coupled cluster calculations for $(112)H^+$, $(112)F_2$, and $(112)F_4$. *J. Chem. Phys.* **106**, 3623–3632 (1997).
84. Seth, M., Cooke, F., Schwerdtfeger, P., Heully, J.-L. & Pelissier, M. The chemistry of the superheavy elements. II. the stability of high oxidation states in group 11 elements: relativistic coupled cluster calculations for the di-, tetra- and hexafluoro metallates of Cu, Ag, Au, and element 111. *J. Chem. Phys.* **109**, 3935–3943 (1998).
85. Schwerdtfeger, P., Dolg, M., Schwarz, W. H. E., Bowmaker, G. A. & Boyd, P. D. W. Relativistic effects in gold chemistry. I. diatomic gold compounds. *J. Chem. Phys.* **91**, 1762–1774 (1989).
86. Söhnel, T., Hermann, H. & Schwerdtfeger, P. Towards the understanding of solid-state structures: From cubic to chainlike arrangements in group 11 halides. *Angew. Chem. Int. Ed.* **40**, 4381–4385 (2001).
87. Pahl, E. & Schwerdtfeger, P. in *Handbook of Nanophysics: Clusters and Fullerenes* Ch. 3 (ed. Sattler, K. D.) 1–13 (CRC Press, 2010).
88. Calvo, F., Pahl, E., Wormit, M. & Schwerdtfeger, P. Evidence for low-temperature melting of mercury owing to relativity. *Angew. Chem. Int. Ed.* **52**, 7583–7585 (2013).
89. Steenbergen, K. G., Pahl, E. & Schwerdtfeger, P. Accurate, large-scale density functional melting of Hg: Relativistic effects decrease melting temperature by 160 K. *J. Phys. Chem. Lett.* **8**, 1407–1412 (2017).
90. Mewes, J.-M., Smits, O. R., Kresse, G. & Schwerdtfeger, P. Copernicium: a relativistic noble liquid. *Angew. Chem. Int. Ed.* **58**, 17964–17968 (2019).
91. Pitzer, K. S. Are elements 112, 114, and 118 relatively inert gases? *J. Chem. Phys.* **63**, 1032–1033 (1975).
92. Gaston, N., Opahle, I., Gäggeler, H. W. & Schwerdtfeger, P. Is eka-mercury (element 112) a group 12 metal? *Angew. Chem. Int. Ed.* **46**, 1663–1666 (2007).
93. Deng, S., Simon, A. & Köhler, J. Superconductivity and chemical bonding in mercury. *Angew. Chem. Int. Ed.* **37**, 640–643 (1998).
94. Kaupp, M. & von Schnering, H. G. Gaseous mercury(IV) fluoride, HgF_4: an ab initio study. *Angew. Chem. Int. Ed.* **32**, 861–863 (1993).
95. Wang, X., Andrews, L., Riedel, S. & Kaupp, M. Mercury is a transition metal: the first experimental evidence for HgF_4. *Angew. Chem. Int. Ed.* **46**, 8371–8375 (2007).

96. Eichler, R. et al. Chemical characterization of element 112. *Nature* **447**, 72–75 (2007).
97. Trombach, L., Ehlert, S., Grimme, S., Schwerdtfeger, P. & Mewes, J.-M. Exploring the chemical nature of super-heavy main-group elements by means of efficient plane-wave density-functional theory. *Phys. Chem. Chem. Phys.* **21**, 18048–18058 (2019).
98. Schwarz, W. H. E. in *Relativistic Methods for Chemists* (eds Barysz, M. & Ishikawa, Y.) 1–62 (Springer, 2010).
99. Froben, F. W., Schulze, W. & Kloss, U. Raman spectra of matrix-isolated group IIIA dimers: Ga_2, In_2, Tl_2. *Chem. Phys. Lett.* **99**, 500–502 (1983).
100. Liu, W., van Wüllen, C., Wang, F. & Li, L. Spectroscopic constants of MH and M_2 (M=Tl, E113, Bi, E115): Direct comparisons of four- and two-component approaches in the framework of relativistic density functional theory. *J. Chem. Phys.* **116**, 3626–3634 (2002).
101. Pershina, V. Relativity in the electronic structure of the heaviest elements and its influence on periodicities in properties. *Radiochim. Acta* **107**, 833–863 (2019).
102. Hermann, A., Furthmüller, J., Gäggeler, H. W. & Schwerdtfeger, P. Spin-orbit effects in structural and electronic properties for the solid state of the group-14 elements from carbon to superheavy element 114. *Phys. Rev. B* **82**, 155116 (2010).
103. Eichler, R. et al. Indication for a volatile element 114. *Radiochim. Acta* **98**, 133–139 (2010).
104. Yakushev, A. et al. Superheavy element flerovium (element 114) is a volatile metal. *Inorg. Chem.* **53**, 1624–1629 (2014).
105. Egdell, R. G., Hotokka, M., Laaksonen, L., Pyykkö, P. & Snijders, J. G. Photoelectron spectra and their relativistic interpretation for gaseous bismuth trihalides. *Chem. Phys.* **72**, 237–247 (1982).
106. Walsh, J. P. S. & Freedman, D. E. High-pressure synthesis: a new frontier in the search for next-generation intermetallic compounds. *Acc. Chem. Res.* **51**, 1315–1323 (2018).
107. Nash, C. S. Atomic and molecular properties of elements 112, 114, and 118. *J. Phys. Chem. A* **109**, 3493–3500 (2005).
108. Nash, C. S. & Bursten, B. E. Spin-orbit coupling versus the VSEPR method: On the possibility of a nonplanar structure for the super-heavy noble gas tetrafluoride $(118)F_4$. *Angew. Chem. Int. Ed.* **38**, 151–153 (1999).
109. Jerabek, P., Smits, O. R., Mewes, J.-M., Peterson, K. A. & Schwerdtfeger, P. Solid oganesson via a many-body interaction expansion based on relativistic coupled-cluster theory and from plane-wave relativistic density functional theory. *J. Phys. Chem. A* **123**, 4201–4211 (2019).
110. Mewes, J.-M., Jerabek, P., Smits, O. R. & Schwerdtfeger, P. Oganesson is a semiconductor: On the relativistic band-gap narrowing in the heaviest noble-gas solids. *Angew. Chem. Int. Ed.* **58**, 14260–14264 (2019).
111. Eliav, E., Kaldor, U., Ishikawa, Y. & Pyykkö, P. Element 118: The first rare gas with an electron affinity. *Phys. Rev. Lett.* **77**, 5350–5352 (1996).
112. Sidgwick, N. V. *The Covalent Link in Chemistry* (Cornell Univ. Press, 1933).
113. Sidgwick, N. V. & Powell, H. M. Bakerian Lecture: stereochemical types and valency groups. *Proc. R. Soc. A* **176**, 153–180 (1940).
114. Schwerdtfeger, P., Heath, G. A., Dolg, M. & Bennett, M. A. Low valencies and periodic trends in heavy element chemistry. a theoretical study of relativistic effects and electron correlation effects in group 13 and period 6 hydrides and halides. *J. Am. Chem. Soc.* **114**, 7518–7527 (1992).
115. Seth, M., Faegri, K. & Schwerdtfeger, P. The stability of the oxidation state +4 in group 14 compounds from carbon to element 114. *Angew. Chem. Int. Ed.* **37**, 2493–2496 (1998).
116. Schwerdtfeger, P. & Seth, M. Relativistic quantum chemistry of the superheavy elements. closed-shell element 114 as a case study. *J. Nucl. Radiochem. Sci.* **3**, 133–136 (2002).
117. Vest, B., Klinkhammer, K., Thierfelder, C., Lein, M. & Schwerdtfeger, P. Kinetic and thermodynamic stability of the group 13 trihydrides. *Inorg. Chem.* **48**, 7953–7961 (2009).
118. Ahuja, R., Blomqvist, A., Larsson, P., Pyykkö, P. & Zaleski-Ejgierd, P. Relativity and the lead-acid battery. *Phys. Rev. Lett.* **106**, 018301 (2011).
119. Roos, B. O. & Pyykkö, P. Bonding trends in molecular compounds of lanthanides: The double-bonded

carbene cations LnCH$_2^+$, Ln = Sc, Y, La-Lu. *Chem. Eur. J.* **16**, 270–275 (2010).

120. Xu, W.-H. et al. Rare-earth monocarbonyls MCO: comprehensive infrared observations and a transparent theoretical interpretation for M=Sc; Y; La-Lu. *Chem. Sci.* **3**, 1548–1554 (2012).

121. Goldschmidt, V. M., Barth, T. F. W., Lunde, G. & Geochemische Verteilungsgesetze der Elemente, V. Isomorphie und Polymorphie der Sesquioxyde: Die Lanthanidenkontraktion und Ihre Konsequenzen. *Skrifter Norske VidenskapsAkad. Oslo I Mat. Naturv. Kl.* **7**, 1–59 (1925).

122. Gao, C. et al. Observation of the asphericity of 4*f*-electron density and its relation to the magnetic anisotropy axis in single-molecule magnets. *Nat. Chem.* **12**, 213–219 (2020).

123. Ryan, A. J. et al. Synthesis, structure, and magnetism of tris(amide) [ln{N(SiMe₃)₂}₃]¹⁻ complexes of the non-traditional +2 lanthanide ions. *Chem. Eur. J.* **24**, 7702–7709 (2018).

124. Kaltsoyannis, N., Hay, P. J., Li, J., Blaudeau, J.-P. & Bursten, B. E. in *The Chemistry of the Actinide and Transactinide Elements* 3rd edn Vol. 3 (eds Morss, L. R., Edelstein, N. M. & Fuger, J.) 1893–2012 (Springer, 2006).

125. Galley, S. S. et al. Synthesis and characterization of tris-chelate complexes for understanding *f*-orbital bonding in later actinides. *J. Am. Chem. Soc.* **141**, 2356–2366 (2019).

126. White, F. D., Dan, D. & Albrecht-Schmitt, T. E. Contemporary chemistry of berkelium and californium. *Chem. Eur. J.* **25**, 10251–10261 (2019).

127. Vitova, T. et al. The role of the 5*f* valence orbitals of early actinides in chemical bonding. *Nat. Commun.* **8**, 16053 (2017).

128. Seth, M., Dolg, M., Fulde, P. & Schwerdtfeger, P. Lanthanide and actinide contractions: relativistic and shell structure effects. *J. Am. Chem. Soc.* **117**, 6597–6598 (1995).

129. Küchle, W., Dolg, M. & Stoll, H. Ab initio study of the lanthanide and actinide contraction. *J. Phys. Chem. A* **101**, 7128–7133 (1997).

130. Chemey, A. T. & Albrecht-Schmitt, T. E. Evolution of the periodic table through the synthesis of new elements. *Radiochim. Acta* **107**, 771–801 (2019).

131. Pyykkö, P. Is the Periodic Table all right ("PT OK")? *EPJ Web Conf.* **131**, 01001 (2016).

132. Münzenberg, G. From bohrium to copernicium and beyond SHE research at SHIP. *Nucl. Phys. A* **944**, 5–29 (2015).

133. Itkis, M., Vardaci, E., Itkis, I., Knyazheva, G. & Kozulin, E. Fusion and fission of heavy and superheavy nuclei (experiment). *Nucl. Phys. A* **944**, 204–237 (2015).

134. Morita, K. SHE research at RIKEN/GARIS. *Nucl. Phys. A* **944**, 30–61 (2015).

135. Dmitriev, S., Itkis, M. & Oganessian, Y. Status and perspectives of the Dubna superheavy element factory. *EPJ Web Conf.* **131**, 08001 (2016).

136. Ball, P. Extreme chemistry: experiments at the edge of the periodic table. *Nature* **565**, 552–555 (2019).

137. Lim, I. S. et al. Relativistic coupled-cluster static dipole polarizabilities of the alkali metals from Li to element 119. *Phys. Rev. A* **60**, 2822–2828 (1999).

138. Schwerdtfeger, P. in *Strength from Weakness: Structural Consequences of Weak Interactions in Molecules, Supermolecules, and Crystals* (eds Domenicano, A. & Hargittai, I.) 169–190 (Springer, 2002).

139. Borschevsky, A., Pershina, V., Eliav, E. & Kaldor, U. Ab initio studies of atomic properties and experimental behavior of element 119 and its lighter homologs. *J. Chem. Phys.* **138**, 124302 (2013).

140. Demidov, Y. A. & Zaitsevskii, A. V. A comparative study of the chemical properties of element 120 and its homologs. *Radiochemistry* **55**, 461–465 (2013).

141. Seaborg, G. T. Prospects for further considerable extension of the periodic table. *J. Chem. Ed.* **46**, 626–634 (1969).

142. Fricke, B., Greiner, W. & Waber, J. T. The continuation of the periodic table up to Z=172. the chemistry of superheavy elements. *Theor. Chim. Acta* **21**, 235–260 (1971).

143. Indelicato, P., Bieroń, J. & Jönsson, P. Are MCDF calculations 101% correct in the super-heavy elements range? *Theor. Chem. Acc.* **129**, 495–505 (2011).

144. Dognon, J.-P. & Pyykkö, P. Chemistry of the 5g elements: Relativistic calculations on hexafluorides. *Angew. Chem. Int. Ed.* **56**, 10132–10134 (2017).

145. Schwerdtfeger, P., Pašteka, L. F., Punnett, A. & Bowman, P. O. Relativistic and quantum electrodynamic effects in superheavy elements. *Nucl. Phys. A* **944**, 551–577 (2015).

146. Grant, I. P. in *Relativistic Effects in Atoms, Molecules, and Solids* (ed. Malli, G. L.) 73–88 (Springer, 1983).

147. Thaller, B. *The Dirac Equation* (Springer, 1992).

148. Pomeranchuk, I. Y. & Smorodinsky, Y. A. On the energy levels of systems with Z>137. *J. Phys. USSR* **9**, 97–100 (1945).

149. Zeldovich, Y. B. & Popov, V. S. Electronic structure of superheavy atoms. *Sov. Phys. Uspekhi* **14**, 673–694 (1972).

150. Reinhardt, J. & Greiner, W. Quantum electrodynamics of strong fields. *Rep. Prog. Phys.* **40**, 219–295 (1977).

151. Maltsev, I. A. et al. How to observe the vacuum decay in low-energy heavy-ion collisions. *Phys. Rev. Lett.* **123**, 113401 (2019).

152. Unsöld, A. & Baschek, B. *The New Cosmos: an Introduction to Astronomy and Astrophysics* (Springer, 2013).

153. Oberhummer, H., Csoto, A. & Schlattl, H. Stellar production rates of carbon and its abundance in the universe. *Science* **289**, 88–90 (2000).

154. Oberhummer, H., Csótó, A. & Schlattl, H. in *The Future of the Universe and the Future of our Civilization* (eds Burdyuzha, V. & Khozin, G.) 197–205 (World Scientific, 2000).

155. Borsanyi, S. et al. Ab initio calculation of the neutron-proton mass difference. *Science* **347**, 1452–1455 (2015).

156. Barrow, J. D. *Impossibility: The Limits of Science and the Science of Limits* (Oxford Univ. Press, 1999).

157. Uzan, J.-P. The fundamental constants and their variation: observational and theoretical status. *Rev. Mod. Phys.* **75**, 403–455 (2003).

158. Pašteka, L. F., Hao, Y., Borschevsky, A., Flambaum, V. V. & Schwerdtfeger, P. Material size dependence on fundamental constants. *Phys. Rev. Lett.* **122**, 160801 (2019).

159. Guggenheimer, K. Remarques sur la constitution des noyaux - II. *J. Phys. Radium* **5**, 475–485 (1934).

160. Guggenheimer, K. Remarques sur la constitution des noyaux atomiques - I. *J. Phys. Radium* **5**, 253–256 (1934).

161. Fea, G. Tabelle riassuntive e bibliografia delle trasmutazioni artificiali. *Il Nuovo Cimento* **12**, 368–406 (1935).

162. Segrè, E. *Nuclei and Particles: an Introduction to Nuclear and Subnuclear Physics* (Benjamin, 1964).

163. Hollander, J. M., Perlman, I. & Seaborg, G. T. Table of isotopes. *Rev. Mod. Phys.* **25**, 469–651 (1953).

164. Strominger, D., Hollander, J. M. & Seaborg, G. T. Table of isotopes. *Rev. Mod. Phys.* **30**, 585–904 (1958).

165. Burbidge, E. M., Burbidge, G. R., Fowler, W. A. & Hoyle, F. Synthesis of the elements in stars. *Rev. Mod. Phys.* **29**, 547–650 (1957).

166. Schatz, H. et al. End point of the *rp* process on accreting neutron stars. *Phys. Rev. Lett.* **86**, 3471–3474 (2001).

167. Pignatari, M., Goebel, K., Reifarth, R. & Travaglio, C. The production of proton-rich isotopes beyond iron: The γ-process in stars. *Int. J. Mod. Phys. E* **25**, 1630003 (2016).

168. Gamow, G. Expanding universe and the origin of elements. *Phys. Rev.* **70**, 572 (1946).

169. Alpher, R. A. & Herman, R. C. Theory of the origin and relative abundance distribution of the elements. *Rev. Mod. Phys.* **22**, 153 (1950).

170. Cirigliano, V. et al. Precision beta decay as a probe of new physics. Preprint at *arXiv* https://arxiv.org/abs/1907.02164 (2019).

171. Yue, A. T. et al. Improved determination of the neutron lifetime. *Phys. Rev. Lett.* **111**, 222501 (2013).

172. Ezhov, V. F. et al. Measurement of the neutron lifetime with ultracold neutrons stored in a magneto-gravitational trap. *JETP Lett.* **107**, 671–675 (2018).

173. Thielemann, F.-K., Eichler, M., Panov, I. & Wehmeyer, B. Neutron star mergers and nucleosynthesis of heavy elements. *Annu. Rev. Nucl. Part. Sci.* **67**, 253–274 (2017).

174. Frebel, A. From nuclei to the cosmos: tracing heavy-element production with the oldest stars. *Annu. Rev. Nucl. Part. Sci.* **68**, 237–269 (2018).

175. Horowitz, C. J. et al. *r*-process nucleosynthesis: connecting rare-isotope beam facilities with the cosmos. *J. Phys. G Nucl. Part. Phys.* **46**, 083001 (2019).

176. Heger, A., Hoffman, R. D., Rauscher, T. & Woosley, S. E. Nucleosynthesis in massive stars with improved nuclear and stellar physics. *Astrophys. J.* **576**, 323–348 (2002).

177. Hampel, M., Stancliffe, R. J., Lugaro, M. & Meyer, B. S. The intermediate neutron-capture process and carbon-enhanced metal-poor stars. *Astrophys. J.* **831**, 171 (2016).

178. Clarkson, O., Herwig, F. & Pignatari, M. Pop III *i*-process nucleosynthesis and the elemental abundances of SMSS J0313-6708 and the most iron-poor stars. *Mon. Not. R. Astron. Soc.* **474**, L37–L41 (2018).

179. Busso, M., Gallino, R. & Wasserburg, G. J. Nucleosynthesis in asymptotic giant branch stars: Relevance for galactic enrichment and solar system formation. *Annu. Rev. Astron. Astrophys.* **37**, 239–309 (1999).

180. Cameron, A. G. Abundances of the elements in the solar system. *Space Sci. Rev.* **15**, 121–146 (1973).

181. Ratzel, U. et al. Nucleosynthesis at the termination point of the *s* process. *Phys. Rev. C* **70**, 065803 (2004).

182. Roederer, I. U. et al. New Hubble Space Telescope observations of heavy elements in four metal-poor stars. *Astrophys. J. Suppl. Ser.* **203**, 27 (2012).

183. Clayton, D. D. *Principles of Stellar Evolution and Nucleosynthesis* (Univ. Chicago Press, 1983).

184. Clayton, D. D., Fowler, W. A., Hull, T. & Zimmerman, B. Neutron capture chains in heavy element synthesis. *Ann. Phys.* **12**, 331–408 (1961).

185. Seeger, P. A., Fowler, W. A. & Clayton, D. D. Nucleosynthesis of heavy elements by neutron capture. *Astrophys. J.* **11**, 121–166 (1965).

186. Arlandini, C. et al. Neutron capture in low-mass asymptotic giant branch stars: cross sections and abundance signatures. *Astrophys. J.* **525**, 886 (1999).

187. Straniero, O., Gallino, R. & Cristallo, S. s process in low-mass asymptotic giant branch stars. *Nucl. Phys. A* **777**, 311–339 (2006).

188. Cristallo, S. et al. Asymptotic-giant-branch models at very low metallicity. *Publ. Astron. Soc. Aust.* **26**, 139–144 (2009).

189. Ulrich, R. in *Explosive nucleosynthesis* (ed. Schramm, D. N. & Arnett, W. D.) 139 (Univ. Texas Press, 1973).

190. Käppeler, F., Gallino, R., Bisterzo, S. & Aoki, W. The *s* process: nuclear physics, stellar models, and observations. *Rev. Mod. Phys.* **83**, 157 (2011).

191. Schwarzschild, M. & Härm, R. Hydrogen mixing by helium-shell flashes. *Astrophys. J.* **150**, 961 (1967).

192. Gallino, R. et al. Evolution and nucleosynthesis in low-mass asymptotic giant branch stars. II. Neutron capture and the s-process. *Astrophys. J.* **497**, 388 (1998).

193. Peters, J. G. Nucleosynthesis by the s-process in stars of 9 and 15 solar masses. *Astrophys. J.* **154**, 225 (1968).

194. Travaglio, C. et al. Galactic chemical evolution of heavy elements: from barium to europium. *Astrophys. J.* **521**, 691 (1999).

195. Travaglio, C. et al. Galactic evolution of Sr, Y, and Zr: a multiplicity of nucleosynthetic processes. *Astrophys. J.* **601**, 864 (2004).

196. Siegel, D. M., Barnes, J. & Metzger, B. D. Collapsars as a major source of r-process elements. *Nature* **569**, 241–244 (2019).

197. Argast, D., Samland, M., Thielemann, F.-K. & Qian, Y.-Z. Neutron star mergers versus core-collapse supernovae as dominant r-process sites in the early galaxy. *Astron. Astrophys.* **416**, 997–1011 (2004).

198. Abbott, B. P. et al. Multi-messenger observations of a binary neutron star merger. *Astrophys. J. Lett.* **848**, L12 (2017).

199. Pian, E. et al. Spectroscopic identification of r-process nucleosynthesis in a double neutron-star merger. *Nature* **551**, 67–70 (2017).

200. Bartos, I. & Marka, S. A nearby neutron-star merger explains the actinide abundances in the early Solar System. *Nature* **569**, 85–88 (2019).

201. Abbott, B. P. et al. GW170817: observation of gravitational waves from a binary neutron star inspiral. *Phys. Rev. Lett.* **119**, 161101 (2017).

202. Cowperthwaite, P. et al. The electromagnetic counterpart of the binary neutron star merger LIGO/Virgo GW170817. II. UV, optical, and near-infrared light curves and comparison to kilonova models. *Astrophys. J. Lett.* **848**, L17 (2017).

203. Holmbeck, E. M. et al. Actinide production in the neutron-rich ejecta of a neutron star merger. *Astrophys. J.* **870**, 23 (2019).

204. Watson, D. et al. Identification of strontium in the merger of two neutron stars. *Nature* **574**, 497–500 (2019).

205. Truran, J. W. Nucleosynthesis. *Annu. Rev. Nucl. Part. Sci.* **34**, 53–97 (1984).

206. Wallerstein, G. et al. Synthesis of the elements in stars: forty years of progress. *Rev. Mod. Phys.* **69**, 995 (1997).

207. Cheifetz, E., Jared, R. C., Giusti, E. R. & Thompson, S. G. Search for superheavy elements in nature. *Phys. Rev. C* **6**, 1348–1361 (1972).

208. Schramm, D. N. Implied superheavy element decay lifetime from meteorites. *Nature* **233**, 258–260 (1971).

209. Köber, E. & Langrock, E. J. Search for superheavy elements in the nature. *Isot. Environ. Health Stud.* **26**, 576–583 (1990).

210. Ter-Akopian, G. M. & Dmitriev, S. N. Searches for superheavy elements in nature: Cosmic-ray nuclei; spontaneous fission. *Nucl. Phys. A* **944**, 177–189 (2015).

211. Petermann, I. et al. Have superheavy elements been produced in nature? *Eur. Phys. J. A* **48**, 122 (2012).

212. Goriely, S. & Pinedo, G. M. The production of transuranium elements by the r-process nucleosynthesis. *Nucl. Phys. A* **944**, 158–176 (2015).

213. Wallner, A. et al. Abundance of live ^{244}Pu in deep-sea reservoirs on Earth points to rarity of actinide nucleosynthesis. *Nat. Commun.* **6**, 5956 (2015).

214. Seaborg, G. T., Mcmillan, E. M., Kennedy, J. W. & Wahl, A. C. Radioactive element 94 from deuterons on uranium. *Phys. Rev.* **69**, 366–367 (1946).

215. Perlman, I. & Seaborg, G. T. The synthetic elements. *Sci. Am.* **182**, 38–47 (1950).

216. Thompson, S. G., Ghiorso, A. & Seaborg, G. T. The new element berkelium (atomic number 97). *Phys. Rev.* **80**, 781–789 (1950).

217. Seaborg, G. T. & Bloom, J. L. The synthetic elements: IV. *Sci. Am.* **220**, 56–69 (1969).

218. Bohr, N. & Wheeler, J. A. The mechanism of nuclear fission. *Phys. Rev.* **56**, 426–450 (1939).

219. Reed, B. C. Simple derivation of the Bohr–Wheeler spontaneous fission limit. *Am. J. Phys.* **71**, 258–260 (2003).

220. Möller, P. The limits of the nuclear chart set by fission and alpha decay. *EPJ Web Conf.* **131**, 03002 (2016).

221. Block, M. et al. Direct mass measurements above uranium bridge the gap to the island of stability. *Nature* **463**, 785–788 (2010).

222. Ramirez, E. M. et al. Direct mapping of nuclear shell effects in the heaviest elements. *Science* **337**, 1207–1210 (2012).

223. Ito, Y. et al. First direct mass measurements of nuclides around Z=100 with a multireflection time-of-flight mass spectrograph. *Phys. Rev. Lett.* **120**, 152501 (2018).

224. Block, M. Direct mass measurements and ionization potential measurements of the actinides. *Radiochim. Acta* **107**, 821–831 (2019).

225. Fischer, C. F. Average-energy-of-configuration Hartree-Fock results for the atoms helium to radon. *At. Data Nucl. Data Tables* **12**, 87–99 (1973).

226. Flambaum, V. V. & Ginges, J. S. M. Radiative potential and calculations of QED radiative corrections to energy levels and electromagnetic amplitudes in many-electron atoms. *Phys. Rev. A* **72**, 052115 (2005).

227. Shabaev, V. M., Tupitsyn, I. I. & Yerokhin, V. A. QEDMOD: Fortran program for calculating the model Lamb-shift operator. *Comput. Phys. Commun.* **189**, 175–181 (2015).

228. Lindgren, I. *Relativistic Many-Body Theory: A New Field-Theoretical Approach* Vol. 63 (Springer, 2016).

229. Sonzogni, A. A. NuDat 2.0: Nuclear structure and decay data on the internet. *AIP Conf. Proc.* **769**, 574–577 (2005).

230. Grochala, W., Hoffmann, R., Feng, J. & Ashcroft, N. W. The chemical imagination at work in *very* tight places. *Angew. Chem. Int. Ed.* **46**, 3620–3642 (2007).

231. Rahm, M., Cammi, R., Ashcroft, N. W. & Hoffmann, R. Squeezing all elements in the periodic table: electron configuration and electronegativity of the atoms under compression. *J. Am. Chem. Soc.* **141**, 10253–10271 (2019).

232. Schwerdtfeger, P. The pseudopotential approximation in electronic structure theory. *ChemPhysChem* **12**, 3143–3155 (2011).

233. Myers, W. D. & Swiatecki, W. Average nuclear properties. *Ann. Phys.* **55**, 395–505 (1969).

234. Nazarewicz, W. Challenges in nuclear structure theory. *J. Phys. G Nucl. Part. Phys.* **43**, 044002 (2016).

235. Weizsäcker, C. F. V. Zur Theorie der Kernmassen. *Zeit. Phys.* **96**, 431–458 (1935).

236. Bethe, H. A. & Bacher, R. F. Nuclear physics A. Stationary states of nuclei. *Rev. Mod. Phys.* **8**, 82–229 (1936).

237. Kaiser, N., Fritsch, S. & Weise, W. Nuclear mean field from chiral pion–nucleon dynamics. *Nucl. Phys. A* **700**, 343–358 (2002).

238. Yamazaki, T., Kuramashi, Y. & Ukawa, A. Helium nuclei in quenched lattice QCD. *Phys. Rev. D* **81**, 111504 (2010).

239. Wiebke, J., Pahl, E. & Schwerdtfeger, P. Melting at high pressure: can first-principles computational chemistry challenge diamond-anvil cell experiments? *Angew. Chem. Int. Ed.* **52**, 13202–13205 (2013).

240. Schwerdtfeger, P., Tonner, R., Moyano, G. E. & Pahl, E. Towards J/mol accuracy for the cohesive energy of solid argon. *Angew. Chem. Int. Ed.* **55**, 12200–12205 (2016).

241. Bartlett, R. J. & Musiał, M. Coupled-cluster theory in quantum chemistry. *Rev. Mod. Phys.* **79**, 291–352 (2007).

242. Coester, F. & Kümmel, H. Short-range correlations in nuclear wave functions. *Nucl. Phys.* **17**, 477–485 (1960).

243. Čížek, J. & Paldus, J. Correlation problems in atomic and molecular systems III. rederivation of the coupled-pair many-electron theory using the traditional quantum chemical methodst. *Int. J. Quantum Chem.* **5**, 359–379 (1971).

244. Kümmel, H. G. A biography of the coupled cluster method. *Int. J. Mod. Phys. B* **17**, 5311–5325 (2003).

245. Kowalski, K., Dean, D. J., Hjorth-Jensen, M., Papenbrock, T. & Piecuch, P. Coupled cluster calculations of ground and excited states of nuclei. *Phys. Rev. Lett.* **92**, 132501 (2004).

246. Hagen, G. et al. Coupled-cluster theory for three-body Hamiltonians. *Phys. Rev. C* **76**, 034302 (2007).

247. Van Dyck, R. S. Jr, Zafonte, S. L., Van Liew, S., Pinegar, D. B. & Schwinberg, P. B. Ultraprecise atomic mass measurement of the α particle and ^{4}He. *Phys. Rev. Lett.* **92**, 220802 (2004).

248. Piecuch, P. & Bartlett, R. J. EOMXCC: A new coupled-cluster method for electronic excited states. *Adv. Quantum Chem.* **34**, 295–380 (1999).

249. Kane, J. V., Pixley, R. E., Schwartz, R. B. & Schwarzschild, A. Lifetimes of the first excited states of F^{17} and O^{17}. *Phys. Rev.* **120**, 162–168 (1960).

250. Gour, J. R., Piecuch, P., Hjorth-Jensen, M., Wloch, M. & Dean, D. J. Coupled-cluster calculations for valence systems around ^{16}O. *Phys. Rev. C* **74**, 024310 (2006).

251. Cottingham, W. N. & Greenwood, D. A. *An Introduction to Nuclear Physics* (Cambridge Univ. Press, 2001).

252. Möller, P., Nix, J. R., Myers, W. D. & Swiatecki, W. J. Nuclear ground-state masses and deformations. *At. Data Nucl. Data Tables* **59**, 185–381 (1995).

253. Moller, P. & Nix, J. R. Stability of heavy and superheavy elements. *J. Phys. G Nucl. Part. Phys.* **20**, 1681–1747 (1994).

254. Sadhukhan, J., Dobaczewski, J., Nazarewicz, W., Sheikh, J. A. & Baran, A. Pairing-induced speedup of nuclear spontaneous fission. *Phys. Rev. C* **90**, 061304 (2014).

255. Bender, M., Heenen, P.-H. & Reinhard, P.-G. Self-consistent mean-field models for nuclear structure. *Rev. Mod. Phys.* **75**, 121 (2003).

256. Rowe, D. J. & Wood, J. L. *Fundamentals of Nuclear Models* (World Scientific, 2010).

257. Zagrebaev, V. I. & Greiner, W. Cross sections for the production of superheavy nuclei. *Nucl. Phys. A* **944**, 257–307 (2015).

258. Oganessian, Y. T., Utyonkov, V. K. & Moody, K. J. Voyage to superheavy island. *Sci. Am.* **282**, 63–67 (2000).

259. Myers, W. D. & Swiatecki, W. J. Nuclear masses and deformations. *Nucl. Phys.* **81**, 1–60 (1966).

260. Ćwiok, S., Heenen, P. H. & Nazarewicz, W. Shape coexistence and triaxiality in the superheavy nuclei. *Nature* **433**, 705–709 (2005).

261. Matheson, Z., Giuliani, S. A., Nazarewicz, W., Sadhukhan, J. & Schunck, N. Cluster radioactivity of $^{294}_{118}$Og$_{176}$. *Phys. Rev. C* **99**, 041304 (2019).

262. Ćwiok, S., Dobaczewski, J., Heenen, P. H., Magierski, P. & Nazarewicz, W. Shell structure of the superheavy elements. *Nucl. Phys. A* **611**, 211–246 (1996).

263. Kruppa, A. T. et al. Shell corrections of superheavy nuclei in self-consistent calculations. *Phys. Rev. C* **61**, 034313 (2000).

264. Morita, K. et al. Experiment on the synthesis of element 113 in the reaction ^{209}Bi(^{70}Zn,n)^{278}113. *J. Phys. Soc. Jpn.* **73**, 2593–2596 (2004).

265. Münzenberg, G. & Morita, K. Synthesis of the heaviest nuclei in cold fusion reactions. *Nucl. Phys. A* **944**, 3–4 (2015).

266. Oganessian, Y. T. et al. Synthesis of the isotopes of elements 118 and 116 in the ^{249}Cf and ^{245}Cm + ^{48}Ca fusion reactions. *Phys. Rev. C* **74**, 044602 (2006).

267. Oganessian, Y. Heaviest nuclei from 48Ca-induced reactions. *J. Phys. G Nucl. Part. Phys.* **34**, R165–R242 (2007).

268. Hofmann, S. Super-heavy nuclei. *J. Phys. G Nucl. Part. Phys.* **42**, 114001 (2015).

269. Kragh, H. The search for superheavy elements: historical and philosophical perspectives. Preprint at *arXiv* https://arxiv.org/abs/1708.04064 (2017).

270. Restrepo, G. Challenges for the periodic systems of elements: chemical, historical and mathematical perspectives. *Chem. Eur. J.* **25**, 15430–15440 (2019).

271. Scerri, E. Can quantum ideas explain chemistry's greatest icon? *Nature* **565**, 557–559 (2019).

272. Scerri, E. & Restrepo, G. *Mendeleev to Oganesson: a Multidisciplinary Perspective on the Periodic Table* (Oxford Univ. Press, 2018).

273. Scerri, E. Cracks in the periodic table. *Sci. Am.* **308**, 68–73 (2013).

274. Scerri, E. R. in *Philosophy of Chemistry. Volume 6 in Handbook of the Philosophy of Science* (eds Woody, A. I., Hendry, R. F. & Needham, P.) 329–338 (North Holland, 2012).

275. Kutzelnigg, W. The periodic table. Its story and its significance. *Int. J. Quantum Chem.* **110**, 1443–1444 (2010).

276. Schädel, M. Chemistry of the superheavy elements. *Philos. Trans. R. Soc. A* **373**, 20140191 (2015).

277. Kirsebom, O. S. et al. Discovery of an exceptionally strong β-decay transition of ^{20}F and implications for the fate of intermediate-mass stars. *Phys. Rev. Lett.* **123**, 262701 (2019).

278. Levi, P. *The Periodic Table* [transl. Rosenthal, R.] (Schocken Books, 1984).

279. Emsley, J. *Nature's building blocks: an A-Z guide to the elements* (Oxford University Press, 2011).

280. Gil, P. The St Andrews Periodic Table. *University of St Andrews* http://special-collections.wp.st-andrews.ac.uk/2019/08/05/the-st-andrews-periodic-table/ (2019).

281. Seaborg, G. T. The periodic table: tortuous path to man-made elements. *Chem. Eng. News* **57**, 46–52 (1979).

282. Haba, H. A new period in superheavy-element hunting. *Nat. Chem.* **11**, 10–13 (2019).

283. Johnson, J. A. Populating the periodic table: nucleosynthesis of the elements. *Science* **363**, 474–478 (2019).

284. Aker, M. et al. Improved upper limit on the neutrino mass from a direct kinematic method by KATRIN. *Phys. Rev. Lett.* **123**, 221802 (2019).

285. Kramida, A., Ralchenko, Y., Reader, J. & NIST ASD Team. NIST Atomic Spectra Database. *NIST* https://physics.nist.gov/asd (2018).

286. Lackenby, B. G. C., Dzuba, V. A. & Flambaum, V. V. Theoretical calculation of atomic properties of superheavy elements Z= 110–112 and their ions. *Phys. Rev. A* **101**, 012514 (2019).

287. Schwerdtfeger, P. & Seth, M. in *Encyclopedia of Computational Chemistry* Vol. 4 (eds Schleyer, P. V. R. et al.) 2480–2499 (Wiley, 1998).

288. Eliav, E., Kaldor, U., Ishikawa, Y., Seth, M. & Pyykkö, P. Calculated energy levels of thallium and eka-thallium (element 113). *Phys. Rev. A* **53**, 3926–3933 (1996).

289. Eliav, E. & Kaldor, U. in *Relativistic Methods for Chemists* (eds Barysz, M. & Ishikawa, Y.) 279–349 (Springer, 2010).

290. Rolfs, C. E., & Rodney, W. S. *Cauldrons in the Cosmos: Nuclear Astrophysics* (Univ. Chicago Press, 1988).

291. Oganessian, Y. T. Synthesis of the heaviest elements in 48Ca-induced reactions. *Radiochim. Acta* **99**, 429–439 (2011).

292. Roederer, I. U. et al. New detections of arsenic, selenium, and other heavy elements in two metal-poor stars. *Astrophys. J.* **791**, 32 (2014).

293. Firsching, F. H. Anomalies in the periodic table. *J. Chem. Educ.* **58**, 478–479 (1981).

294. Meyer, L. Die Natur der chemischen elemente als funktion ihrer atomgewichte. *Annalen Chem. Pharm.* **7**, 354–364 (1870).

295. van Spronsen, J. W. The priority conflict between Mendeleev and Meyer. *J. Chem. Ed.* **46**, 136–139 (1969).

296. Kuhn, N. & Zeller, K.-P. Lothar Meyer-eine Wiederentdeckung. *Nachr. Chem.* **67**, 19–25 (2019).

297. Boeck, G. Das Periodensystem der Elemente und Lothar Meyer. *Chem. Unserer Zeit* **53**, 372–382 (2019).

298. Schwerdtfeger, P. Relativistic and electron-correlation contributions in atomic and molecular properties: benchmark calculations on Au and Au₂. *Chem. Phys. Lett.* **183**, 457–463 (1991).

299. Schwerdtfeger, P. Relativistic effects in properties of gold. *Heteroat. Chem.* **13**, 578–584 (2002).

300. Pyykkö, P. Theoretical chemistry of gold. *Angew. Chem. Int. Ed.* **43**, 4412–4456 (2004).

301. Glantschnig, K. & Ambrosch-Draxl, C. Relativistic effects on the linear optical properties of Au, Pt, Pb and W. *New J. Phys.* **12**, 103048 (2010).

302. Schwerdtfeger, P. Gold goes nano - from small clusters to low-dimensional assemblies. *Angew. Chem. Int. Ed.* **42**, 1892–1895 (2003).

303. Theilacker, K., Schlegel, H. B., Kaupp, M. & Schwerdtfeger, P. Relativistic and solvation effects on the stability of gold(III) halides in aqueous solution. *Inorg. Chem.* **54**, 9869–9875 (2015).

304. Hashmi, A. S. K. The catalysis gold rush: New claims. *Angew. Chem. Int. Ed.* **44**, 6990–6993 (2005).

305. Gorin, D. J. & Toste, F. D. Relativistic effects in homogeneous gold catalysis. *Nature* **446**, 395–403 (2007).

306. Jones, K. L. & Nazarewicz, W. Designer nuclei — making atoms that barely exist. *The Physics Teacher* **48**, 381 (2010).

Competing interests

The authors declare no competing interests.

Publisher's note

Springer Nature remains neutral with regard to jurisdictional claims in published maps and institutional affiliations.

RELATED LINKS

Internet database of periodic tables: https://www.meta-synthesis.com/webbook/35pt/ptdatabase.php
National Nuclear Data Center's NuDat 2 database: http://www.nndc.bnl.gov